Supplementary material

Stable lithium storage with strong-grain sustained pinning-reinforced nanocrystalline silicon

Tingjie Hu, [a] *Haochen Zhou,* [b] *Jingjing Tang,* [a] *Song Chen,* [c] *Zhenxiao Li,* [a] *Xia Yu,* [a] *Yaguang Zhang,* [a] *Juan Yang*[*a] *and Xiangyang Zhou*[*a]

[a] School of Metallurgy and Environment, Central South University, Changsha 410083, China. E-mail: j-yang@csu.edu.cn, 130301@csu.edu.cn

[b] Department of Materials, Imperial College London, London SW7 2AZ, UK.

[c] Hunan Chenyu-Fuji New Energy Technology Co. Ltd., Changde 415100, China.

Supplementary Figures

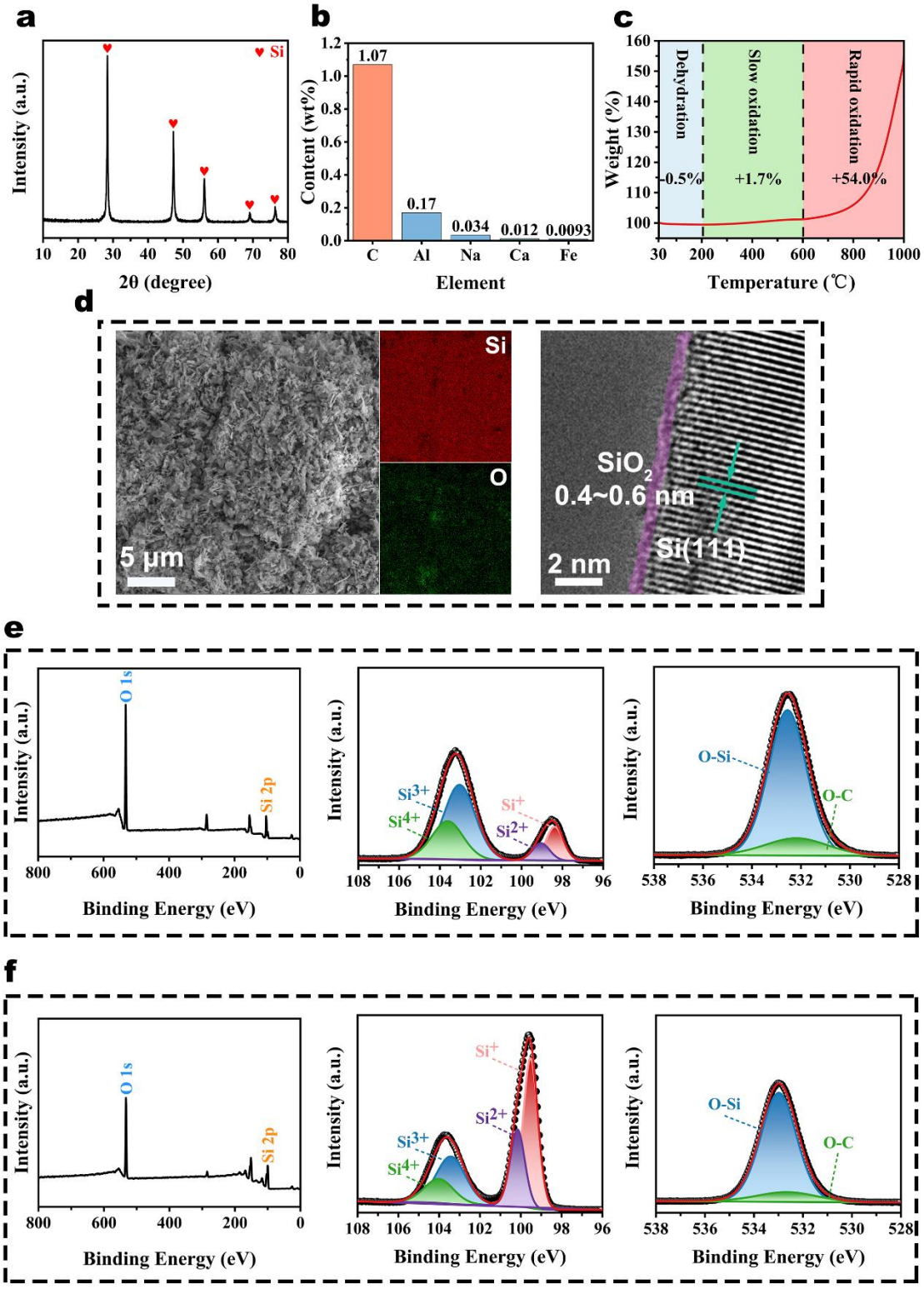

Fig. S1. Purification results. a, XRD spectra of SCNS. **b,** The content of the main impurity elements (C, Al, Na, Ca, Fe) in SCNS. **c,** Thermogravimetric curve of SCNS.

d, SEM, Si and O mapping, and HRTEM of SCNS were employed to observe its micro-morphology and oxygen removal. **e-f,** XPS, and fitted XPS of Si 2p and O 1s were used to analyze the oxidation of Si-raw (**e**) and SCNS (**f**). Obviously after purification, organics, metals, and oxide layers are well removed, yielding SCNS of high purity.

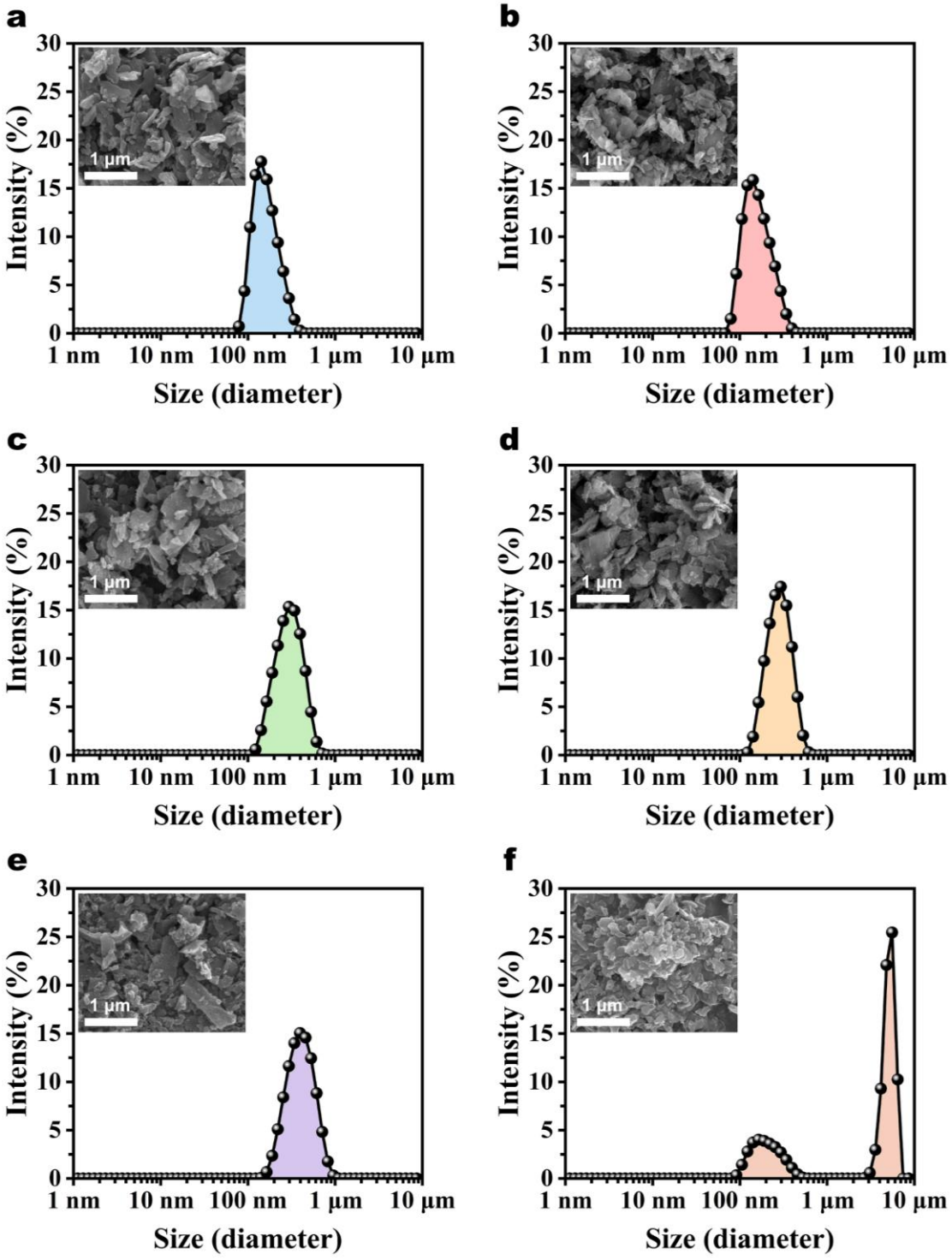

Fig. S2. Particle size distribution of the samples. a-f, The particle size distributions of SCNS (**a**), SCNS-800 (**b**), SCNS-900 (**c**), SCNS-1000 (**d**), SCNS-1100 (**e**) and

SCNS-1200 (**f**) were measured by the particle size analyzer and supplemented with SEM for better observation. With the annealing temperature rising, the particle size of the samples gradually increases and SCNS-1200 even shows the phenomenon of molten agglomeration. This is attributed to the high surface-reactivity of the nanoparticles, which makes the melting phenomenon occur earlier than the melting point.

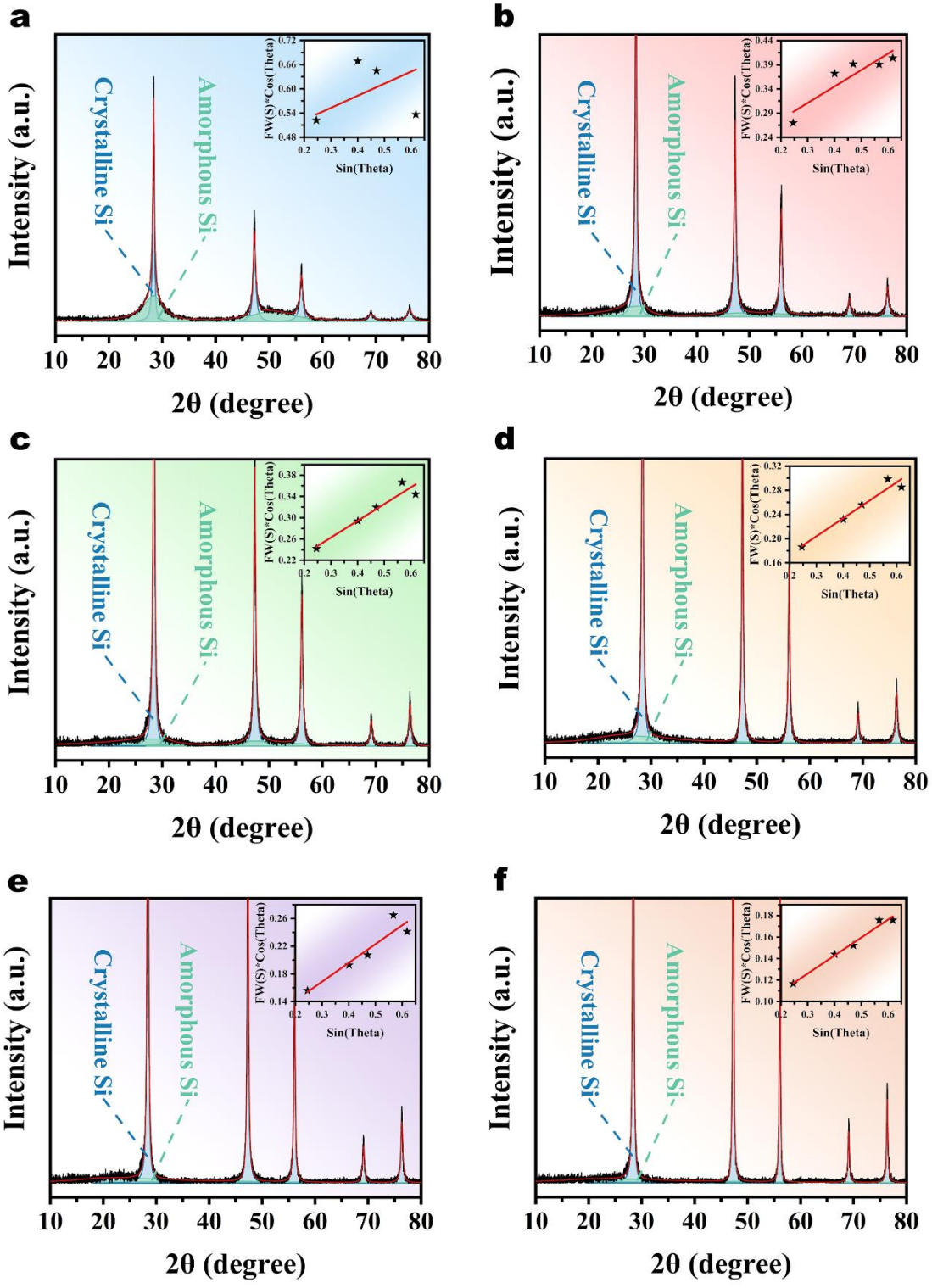

Fig. S3. XRD fitting results. a-f, The crystallinity, grain size and microstrain fitting results of SCNS (**a**), SCNS-800 (**b**), SCNS-900 (**c**), SCNS-1000 (**d**), SCNS-1100 (**e**) and SCNS-1200 (**f**) on the basis of their XRD data.

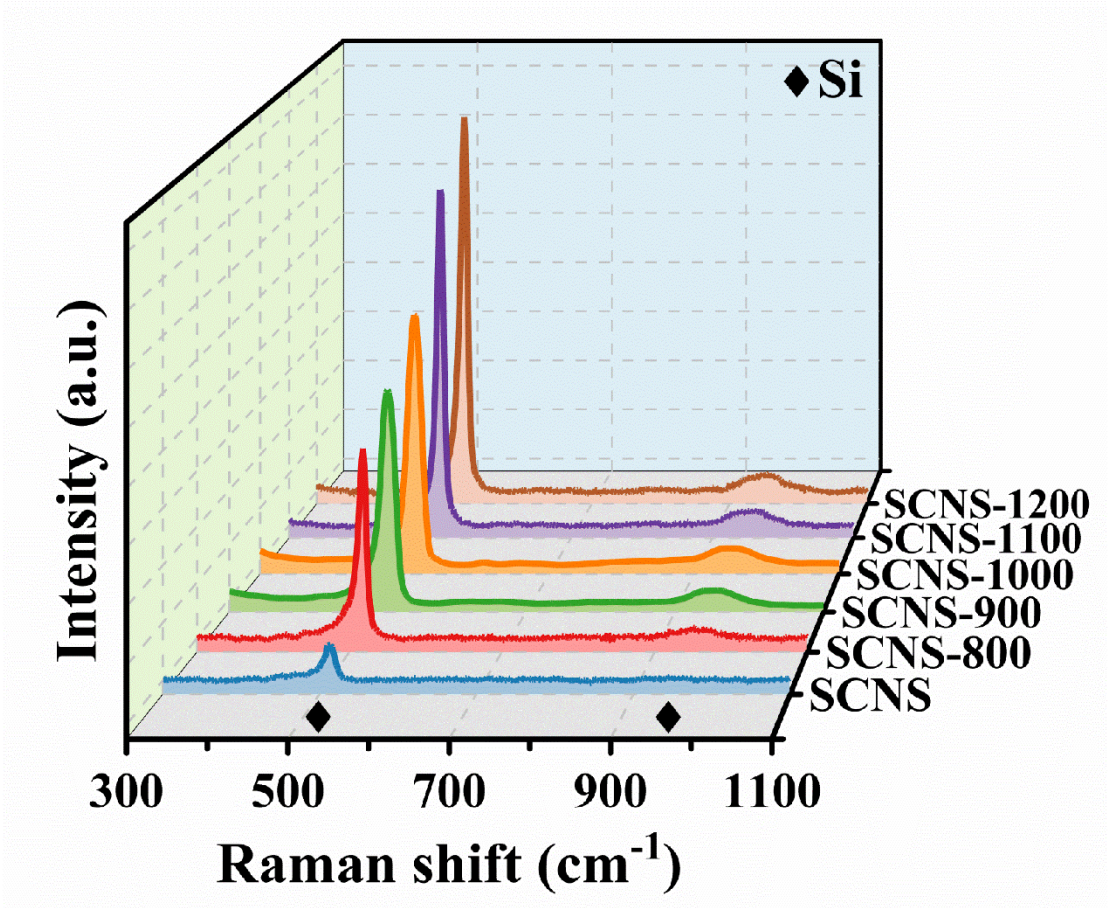

Fig. S4. Raman spectra of the samples were employed to assist in the physical phase characterization.

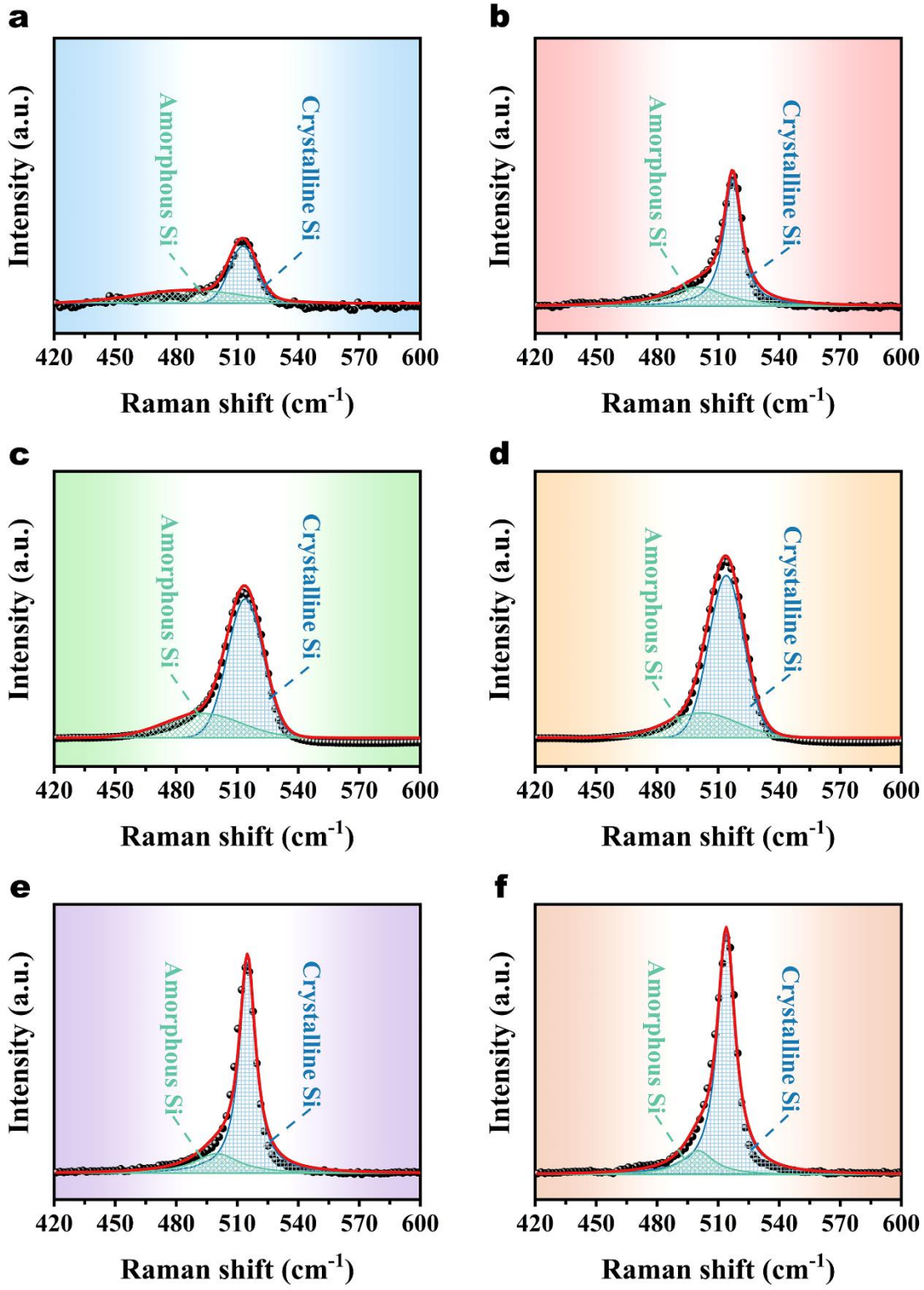

Fig. S5. Raman fitting results (420-600 cm^{-1}). a-f, The crystallinity fitting results of SCNS (**a**), SCNS-800 (**b**), SCNS-900 (**c**), SCNS-1000 (**d**), SCNS-1100 (**e**) and SCNS-1200 (**f**) based on their Raman data.

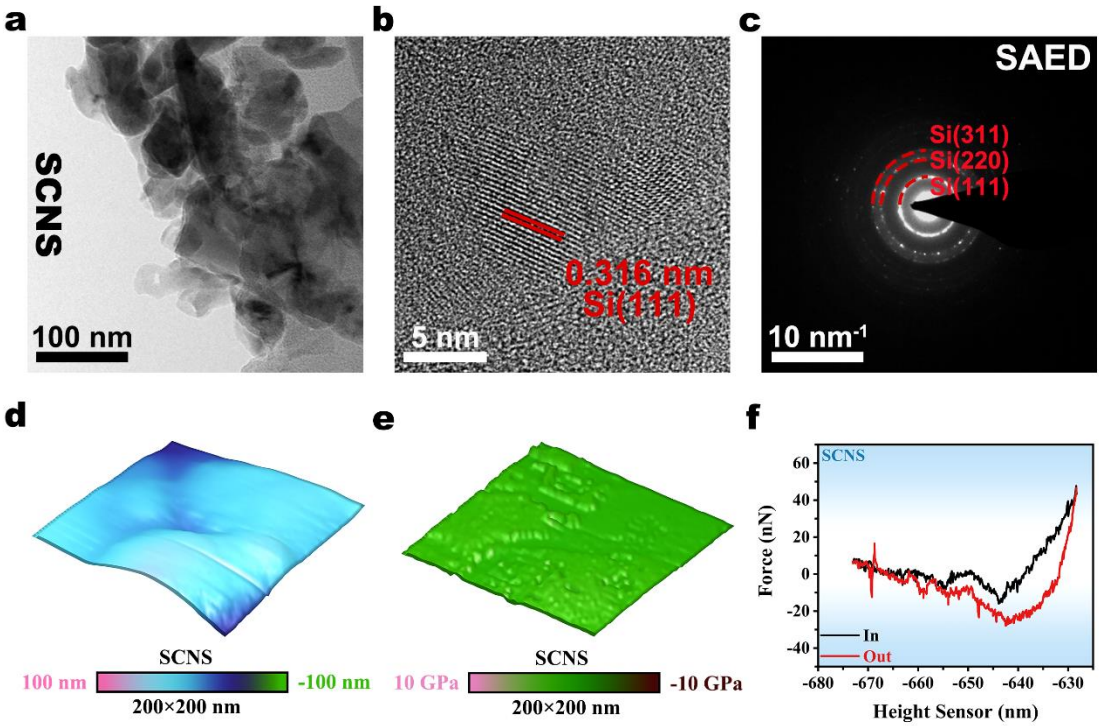

Fig. S6. AC-TEM and AFM characterization of SCNS. a-c, The ultramicroscopic morphology (**a**), crystal structure (**b**) and crystallographic properties (**c**) were observed by TEM, HRTEM and SAED, respectively. **d-f,** The micro 3D morphology (**d**), Young's modulus distribution (**e**) and force curve (**f**) were measured by AFM.

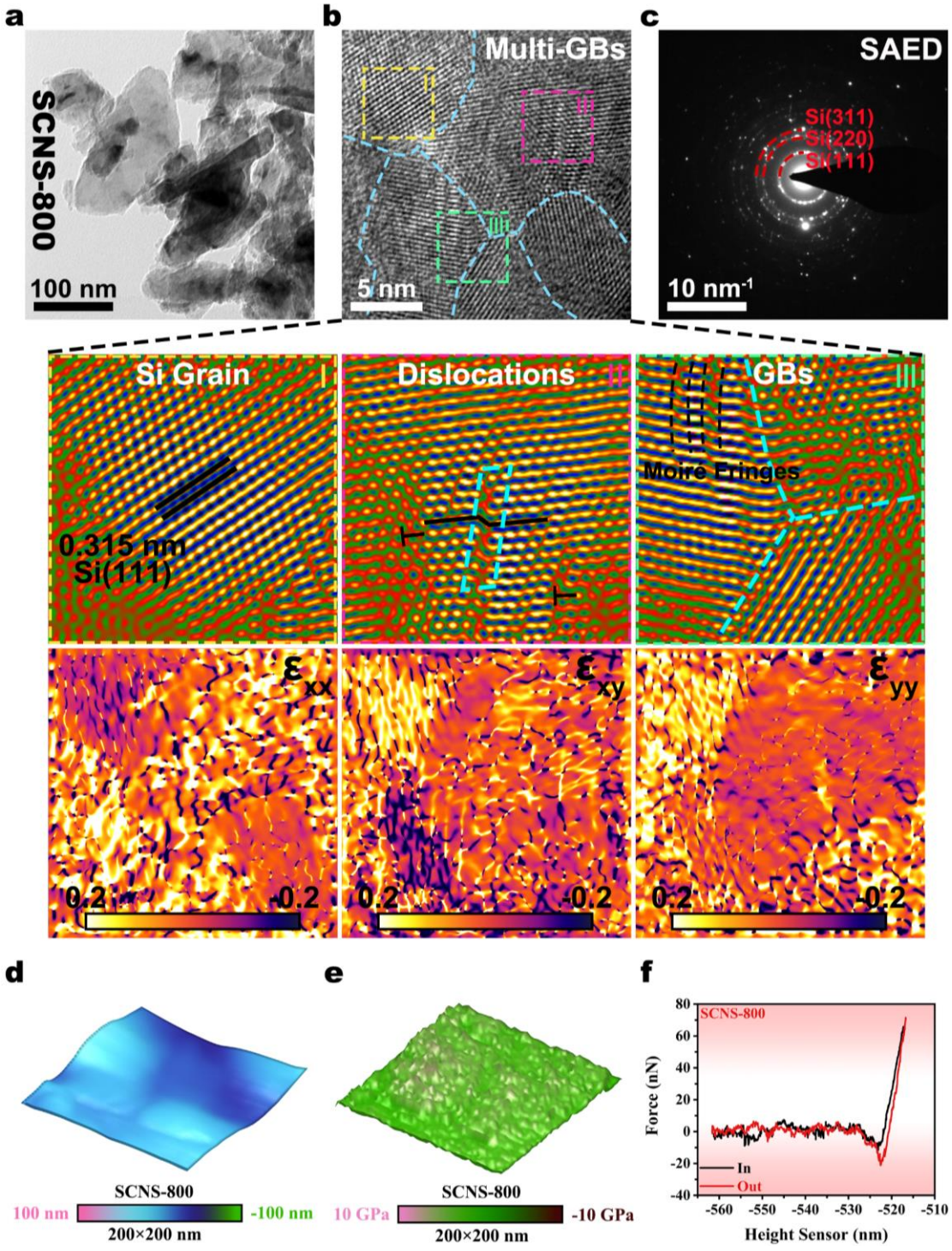

Fig. S7. AC-TEM and AFM characterization of SCNS-800. a-c, The ultramicroscopic morphology (**a**), crystal structure (**b**) and crystallographic properties (**c**) were observed by TEM, HRTEM and SAED, respectively. In addition, regions I, II and III in the HRTEM were filtered by FFT and inverse FFT (IFFT), while the GPA method was used to map the ε_{xx}, ε_{xy} and ε_{yy} microstrain distributions in the HRTEM. **d-f,** The micro 3D morphology (**d**), Young's modulus distribution (**e**) and force curve (**f**)

were measured by AFM.

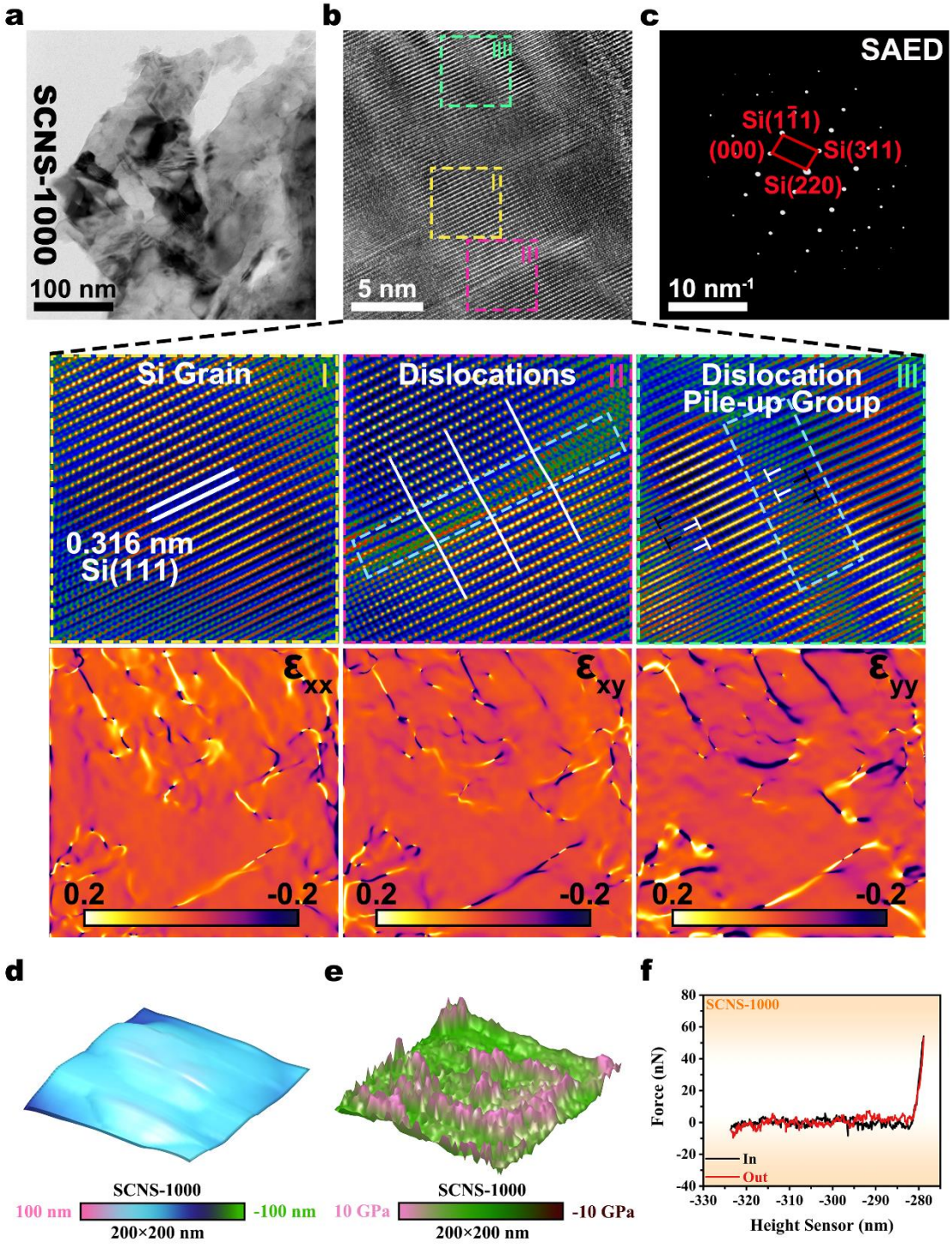

Fig. S8. AC-TEM and AFM characterization of SCNS-1000. a-c, The ultramicroscopic morphology (**a**), crystal structure (**b**) and crystallographic properties (**c**) were observed by TEM, HRTEM and SAED, respectively. In addition, regions I, II and III in the HRTEM were filtered by FFT and IFFT, while the GPA method was used to map the ε_{xx}, ε_{xy} and ε_{yy} microstrain distributions in the HRTEM. **d-f,** The micro 3D

morphology (**d**), Young's modulus distribution (**e**) and force curve (**f**) were measured by AFM.

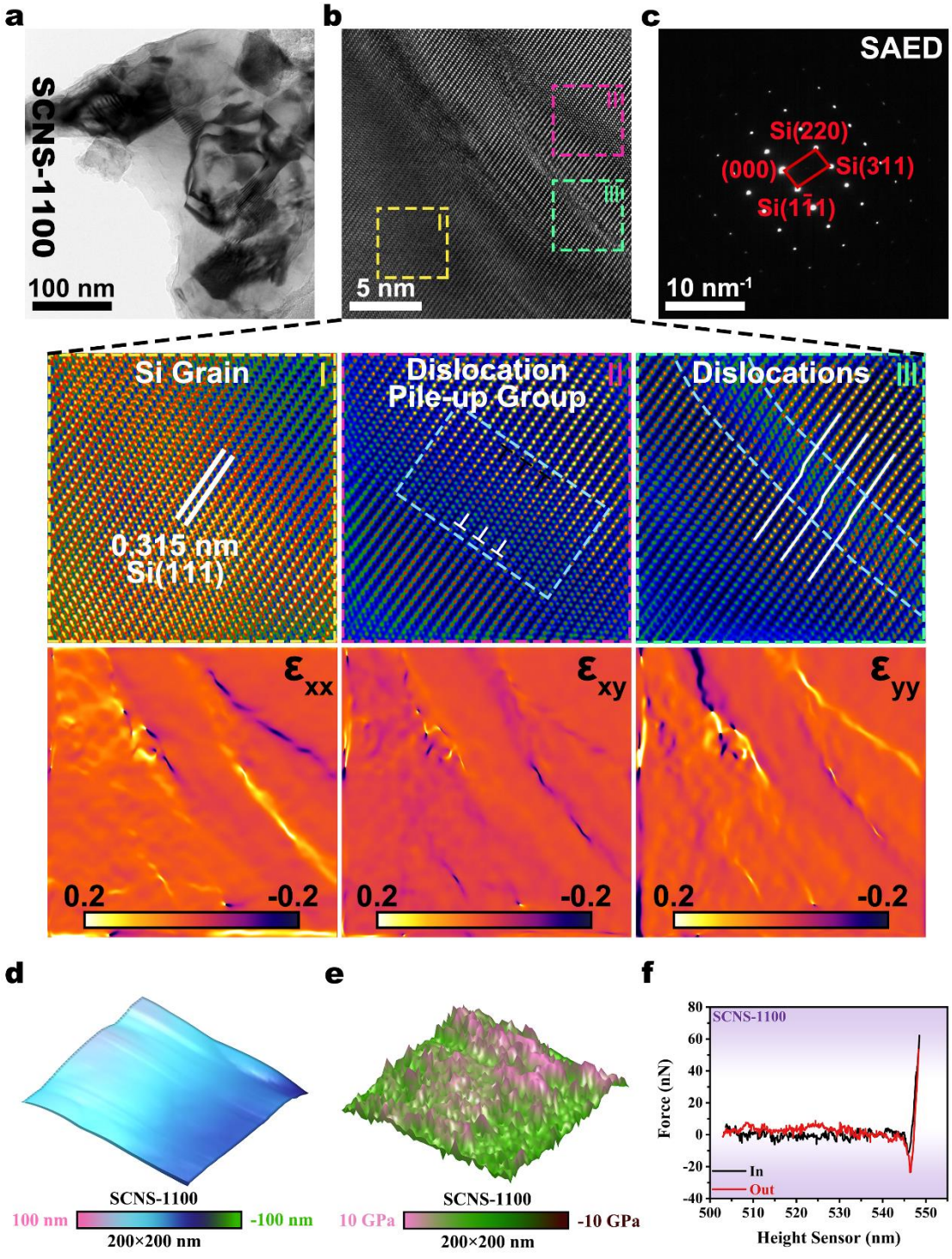

Fig. S9. AC-TEM and AFM characterization of SCNS-1100. a-c, The ultramicroscopic morphology (**a**), crystal structure (**b**) and crystallographic properties (**c**) were observed by TEM, HRTEM and SAED, respectively. In addition, regions I, II and III in the HRTEM were filtered by FFT and IFFT, while the GPA method was used

to map the ε_{xx}, ε_{xy} and ε_{yy} microstrain distributions in the HRTEM. **d-f,** The micro 3D morphology (**d**), Young's modulus distribution (**e**) and force curve (**f**) were measured by AFM.

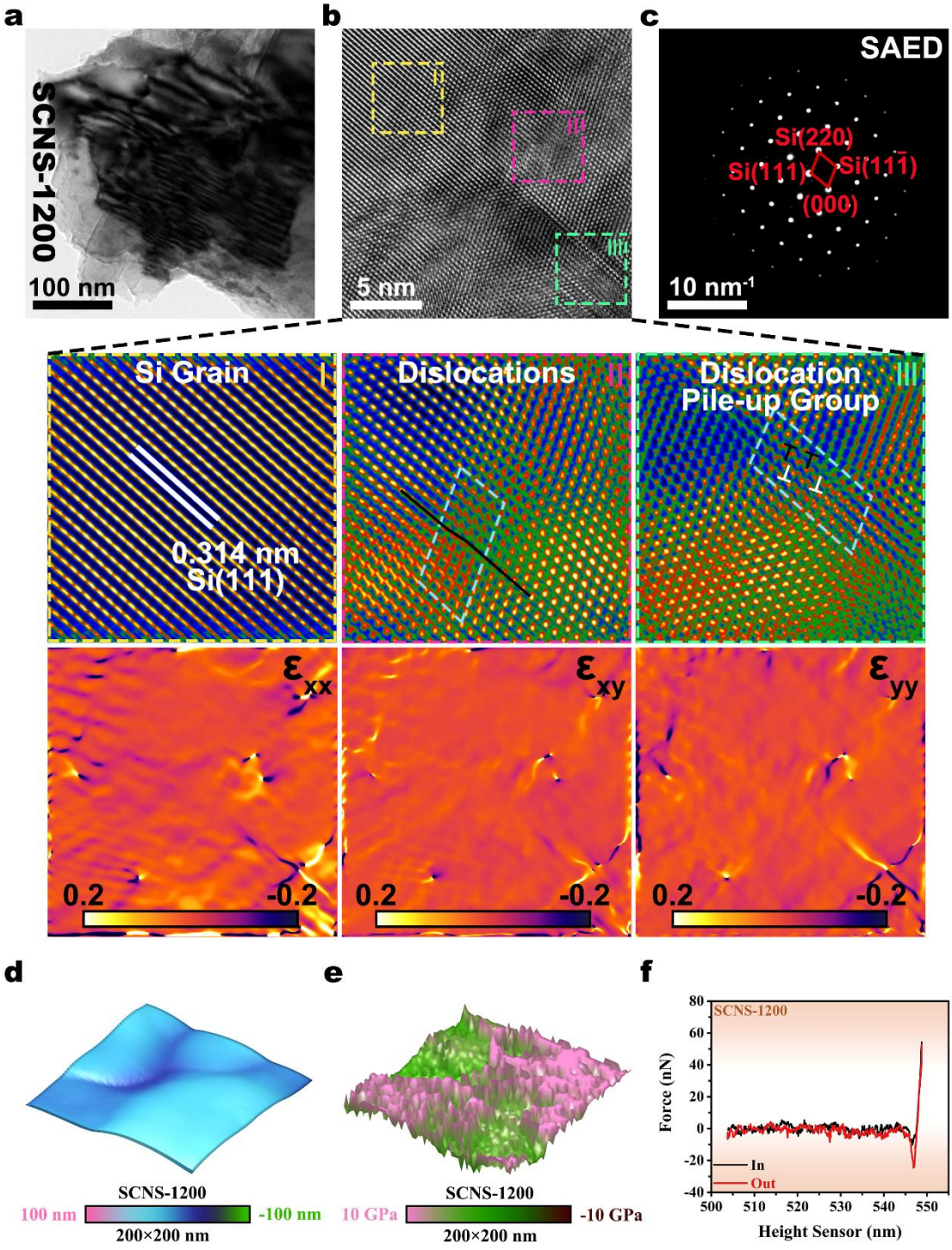

Fig. S10. AC-TEM and AFM characterization of SCNS-1200. a-c, The ultramicroscopic morphology (**a**), crystal structure (**b**) and crystallographic properties (**c**) were observed by TEM, HRTEM and SAED, respectively. In addition, regions I, II

and III in the HRTEM were filtered by FFT and IFFT, while the GPA method was used to map the ε_{xx}, ε_{xy} and ε_{yy} microstrain distributions in the HRTEM. **d-f,** The micro 3D morphology (**d**), Young's modulus distribution (**e**) and force curve (**f**) were measured by AFM.

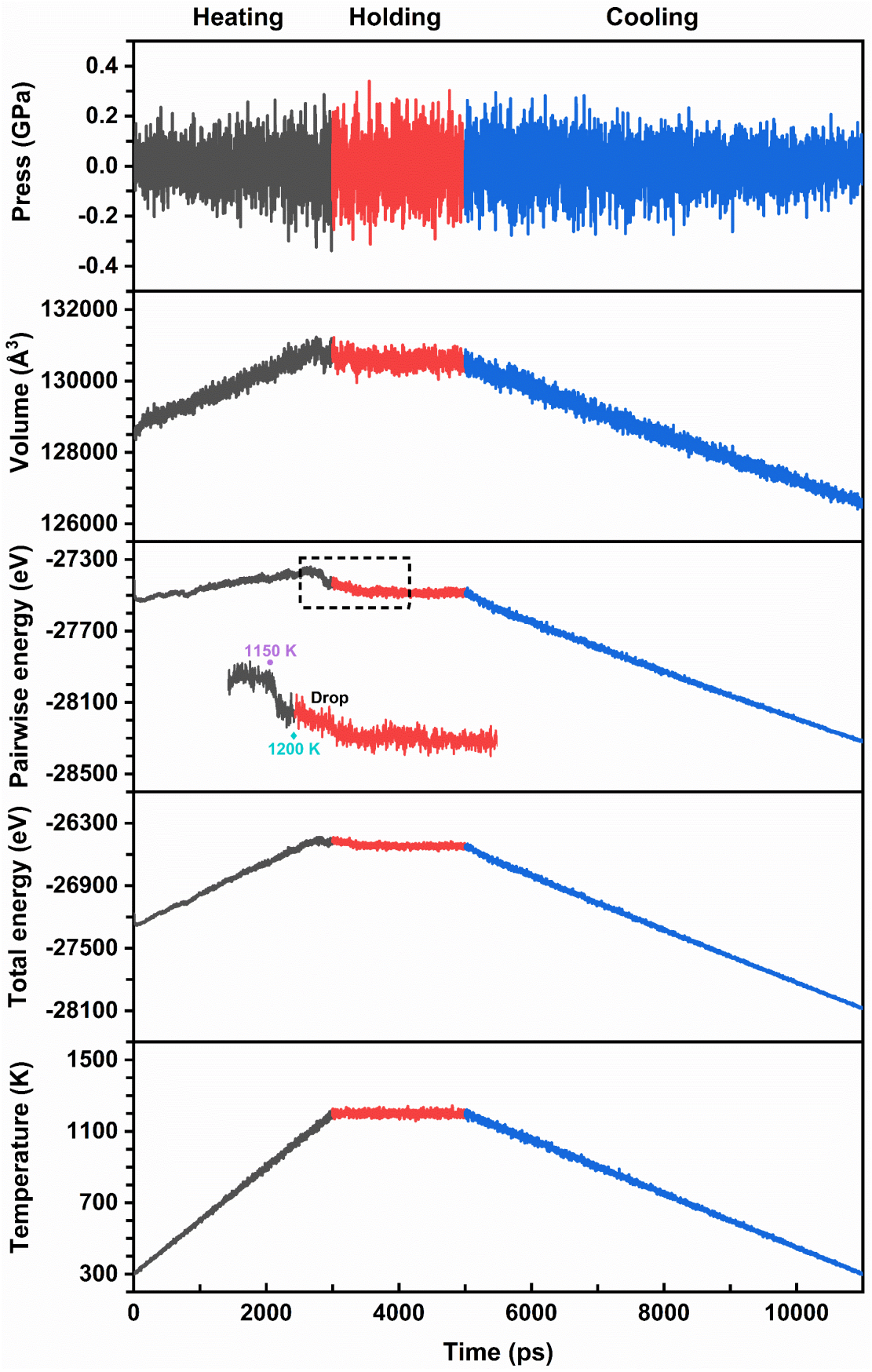

Fig. S11. Curves of temperature, total energy (kinetic and potential), pairwise energy, volume and press of the system in the molecular dynamics simulation of

the annealing process for the generation of SCNS-900.

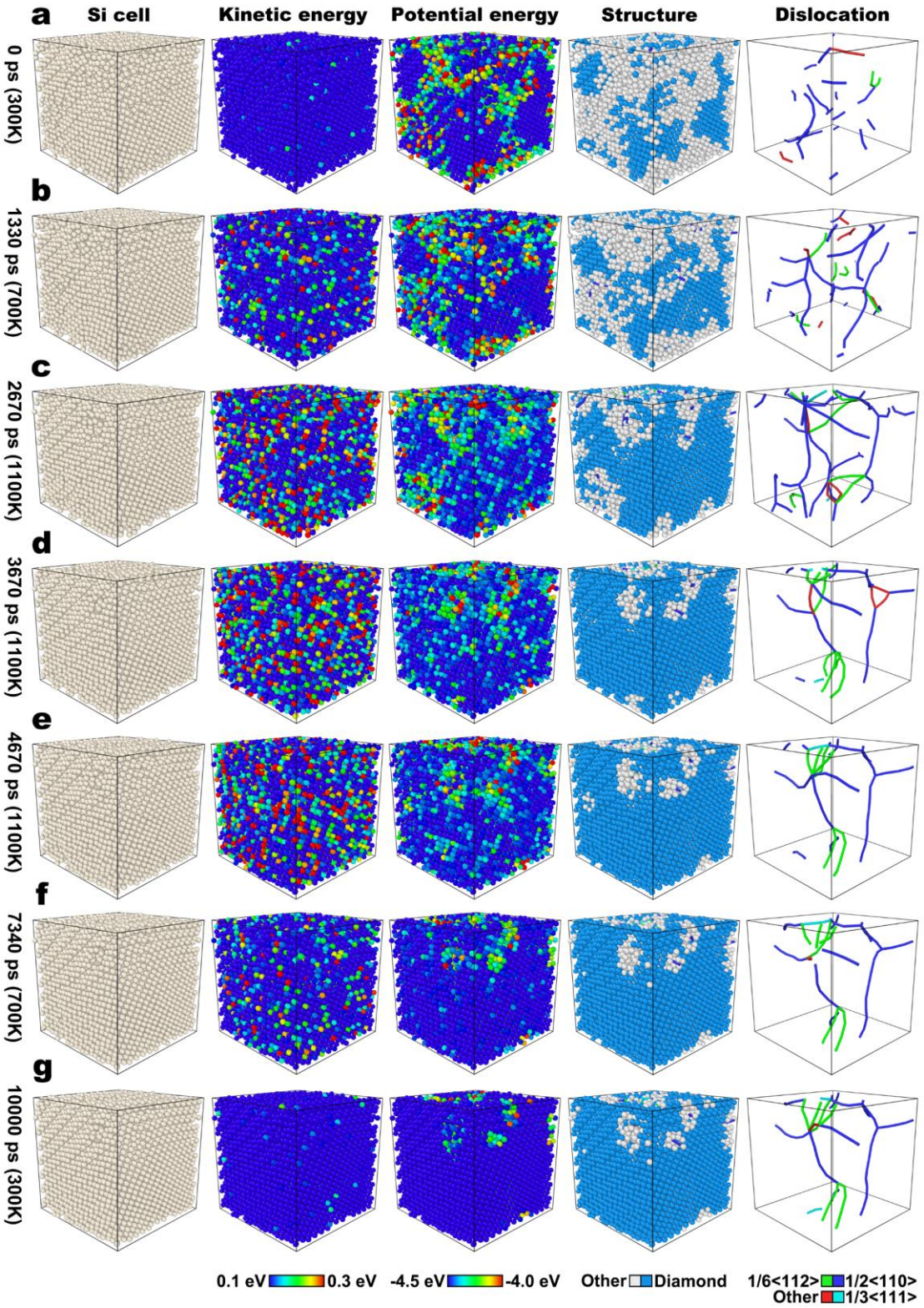

Fig. S12. Molecular dynamics simulation demonstration of the annealing process for the generation of SCNS-800. a-g, Visualization of cell, kinetic energy, potential energy, structure and dislocation for the model at 0 ps (**a**), 1330 ps (**b**), 2670 ps (**c**),

3670 ps (**d**), 4670 ps (**e**), 7340 ps (**f**), and 10000 ps (**g**), respectively.

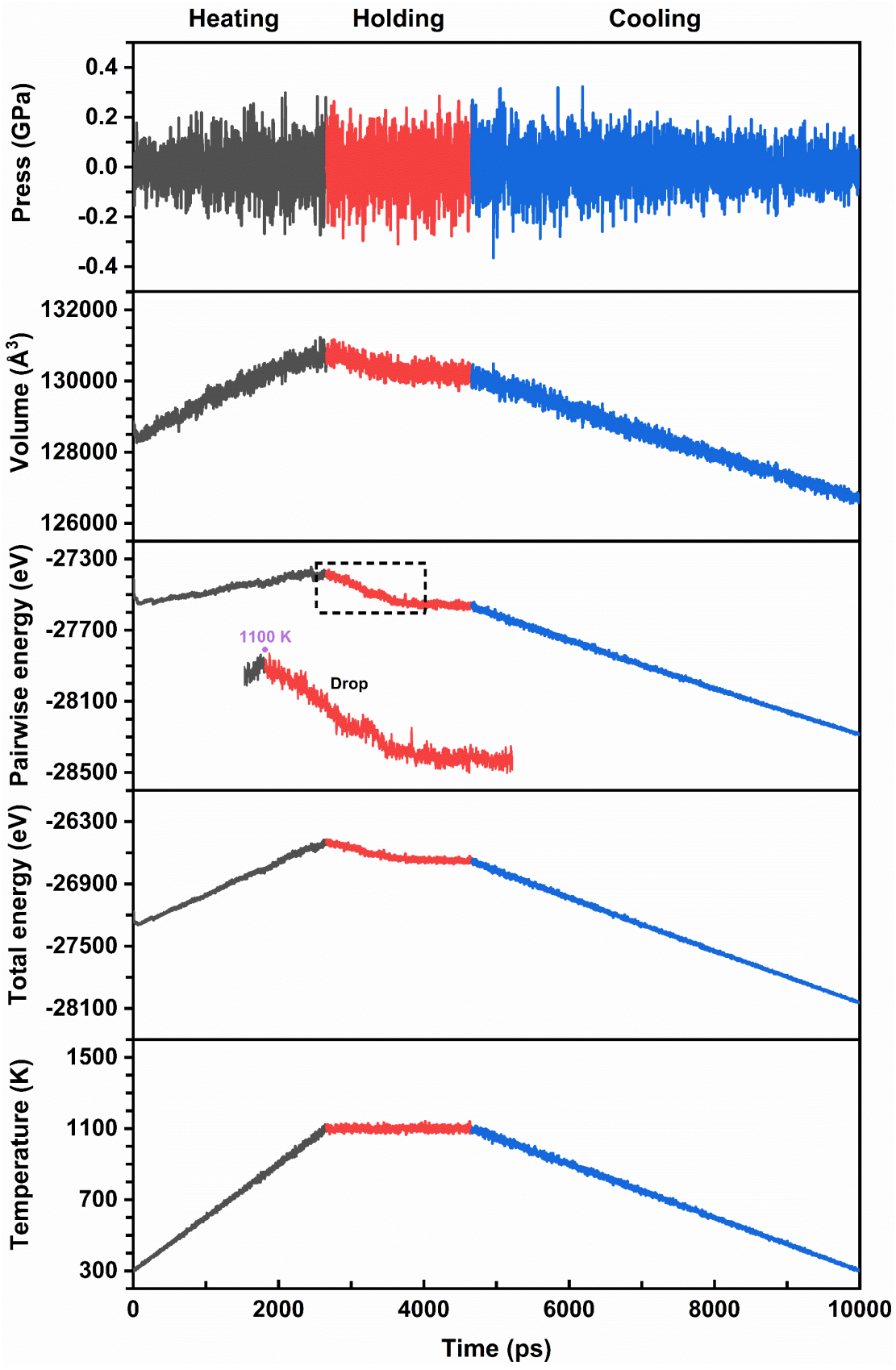

Fig. S13. Curves of temperature, total energy (kinetic and potential), pairwise

energy, volume and press of the system in the molecular dynamics simulation of the annealing process for the generation of SCNS-800.

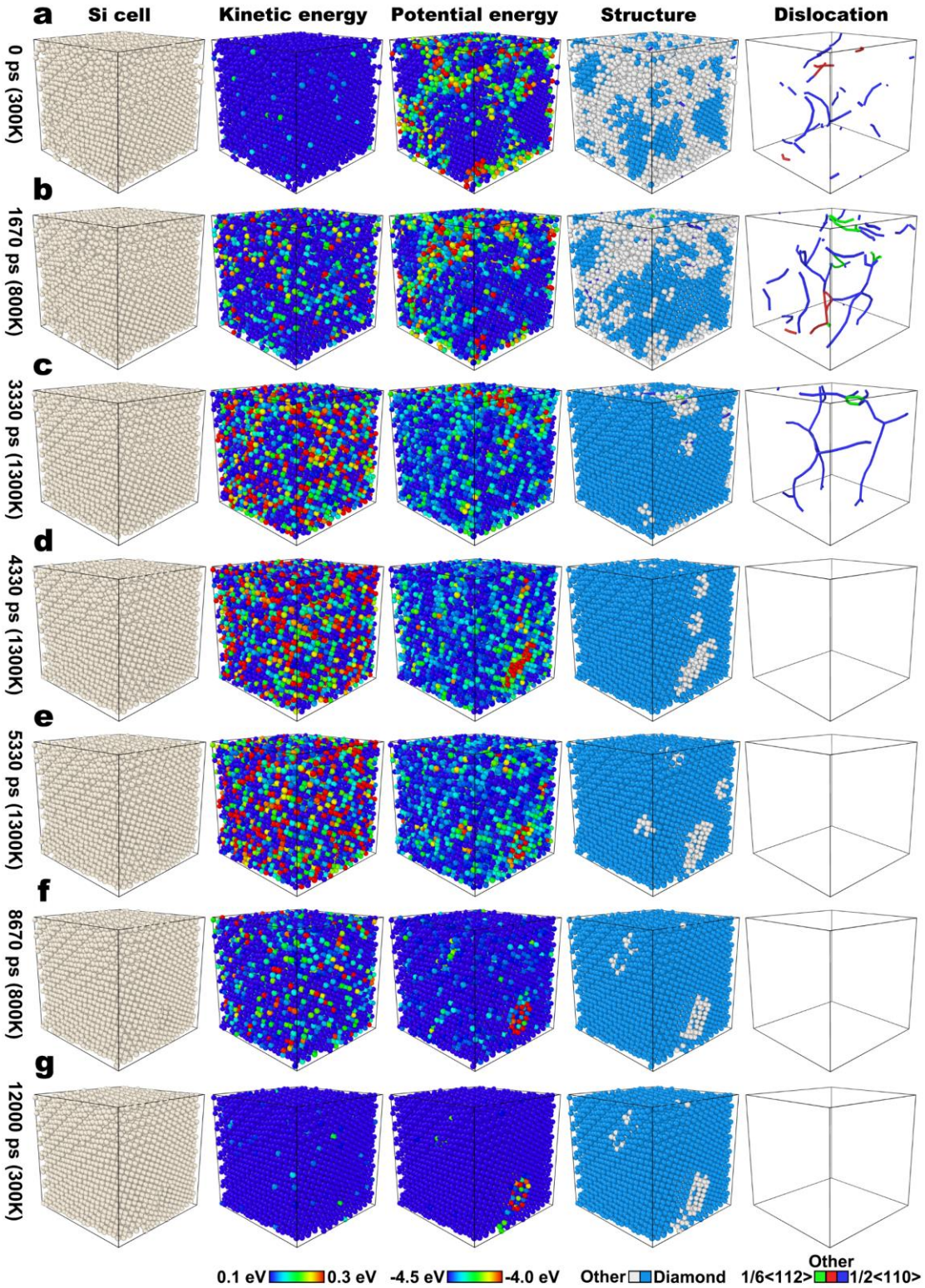

Fig. S14. Molecular dynamics simulation demonstration of the annealing process for the generation of SCNS-1000. a-g, Visualization of cell, kinetic energy, potential

energy, structure and dislocation for the model at 0 ps (**a**), 1670 ps (**b**), 3330 ps (**c**), 4330 ps (**d**), 5330 ps (**e**), 8670 ps (**f**), and 12000 ps (**g**), respectively.

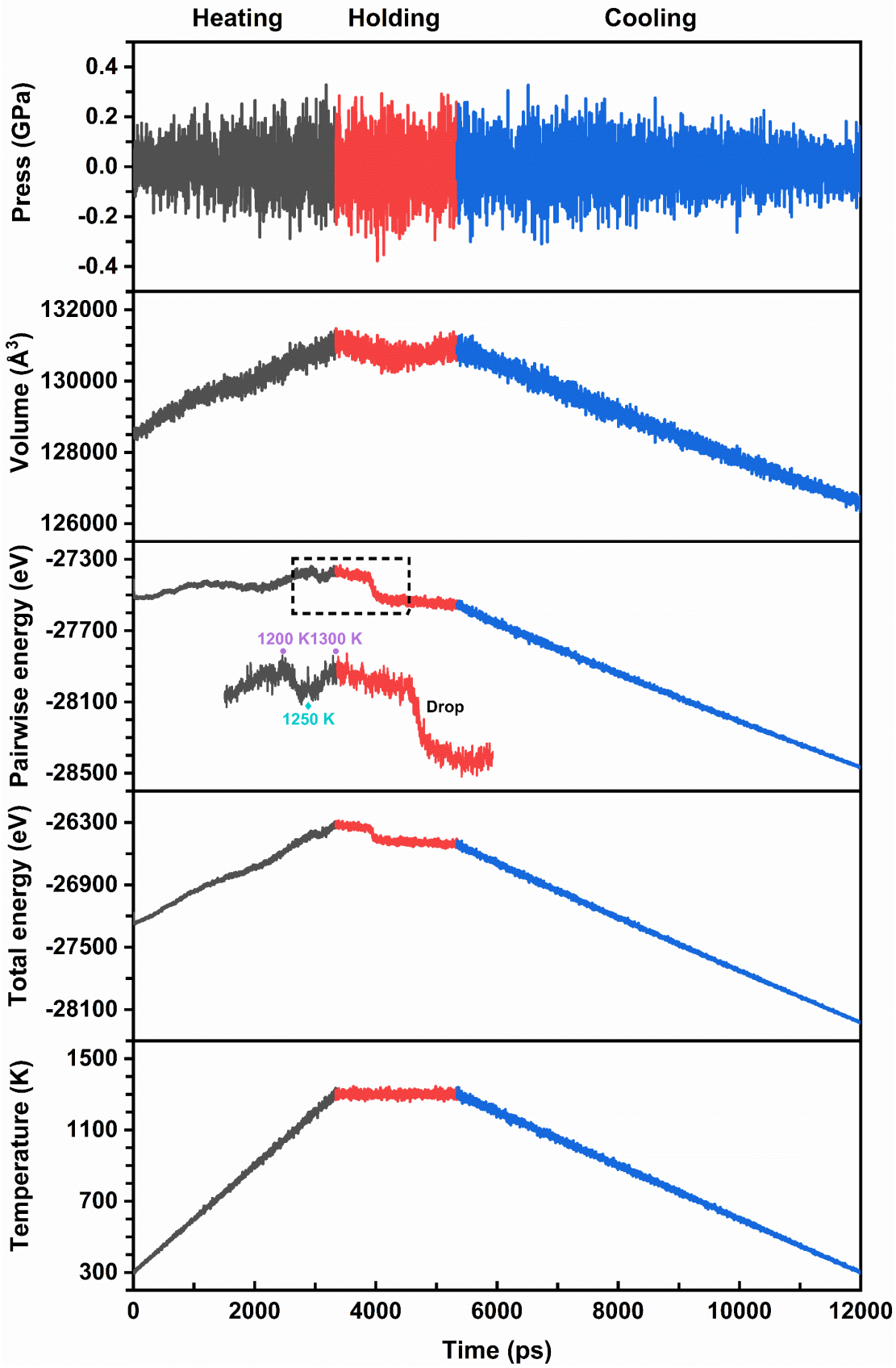

Fig. S15. Curves of temperature, total energy (kinetic and potential), pairwise energy, volume and press of the system in the molecular dynamics simulation of the annealing process for the generation of SCNS-1000.

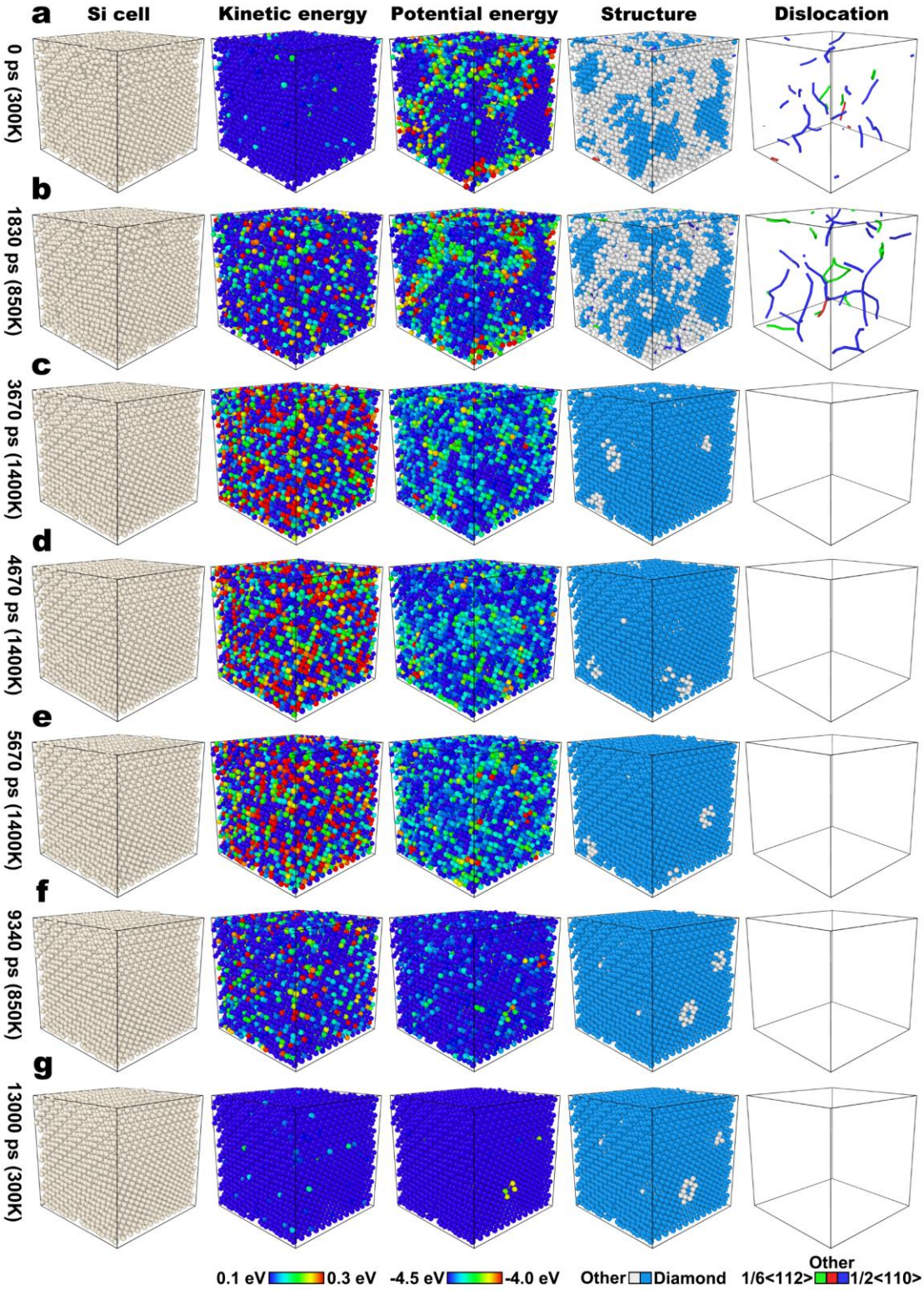

Fig. S16. Molecular dynamics simulation demonstration of the annealing process

for the generation of SCNS-1100. a-g, Visualization of cell, kinetic energy, potential energy, structure and dislocation for the model at 0 ps (**a**), 1830 ps (**b**), 3670 ps (**c**), 4670 ps (**d**), 5670 ps (**e**), 9340 ps (**f**), and 13000 ps (**g**), respectively.

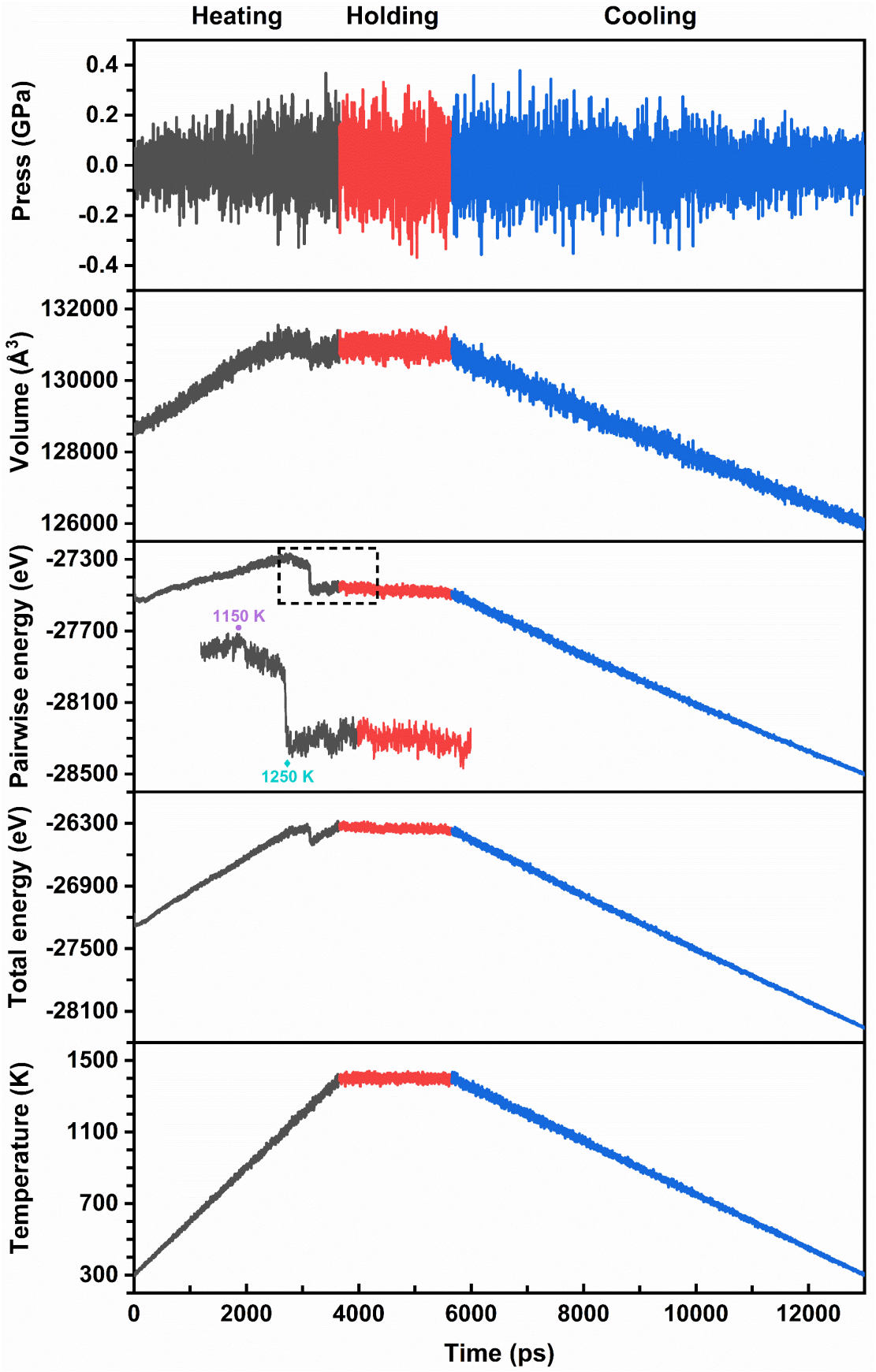

Fig. S17. Curves of temperature, total energy (kinetic and potential), pairwise energy, volume and press of the system in the molecular dynamics simulation of

the annealing process for the generation of SCNS-1100.

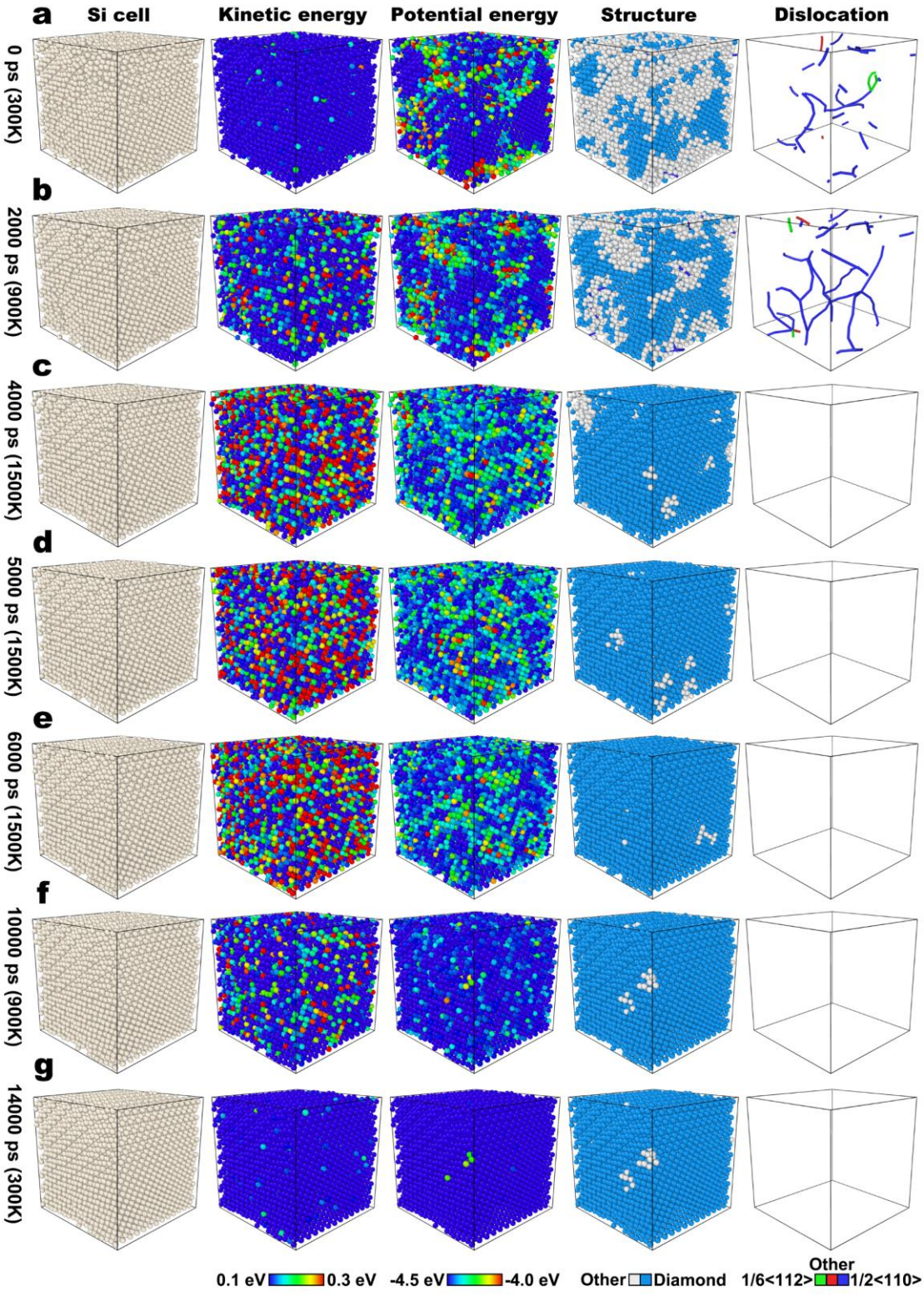

Fig. S18. Molecular dynamics simulation demonstration of the annealing process for the generation of SCNS-1200. a-g, Visualization of cell, kinetic energy, potential energy, structure and dislocation for the model at 0 ps (**a**), 2000 ps (**b**), 4000 ps (**c**),

5000 ps (**d**), 6000 ps (**e**), 10000 ps (**f**), and 14000 ps (**g**), respectively.

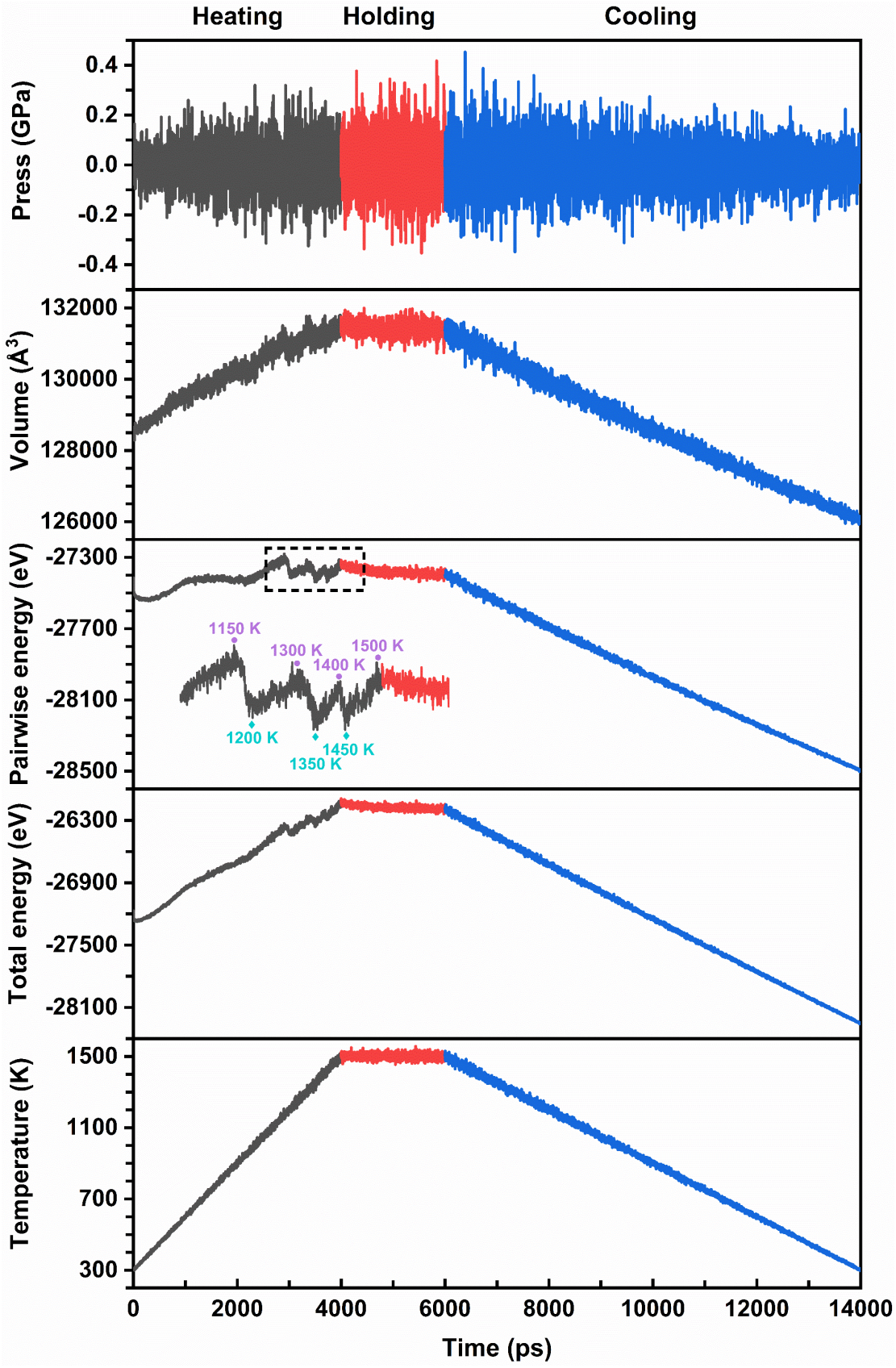

Fig. S19. Curves of temperature, total energy (kinetic and potential), pairwise

energy, volume and press of the system in the molecular dynamics simulation of the annealing process for the generation of SCNS-1200.

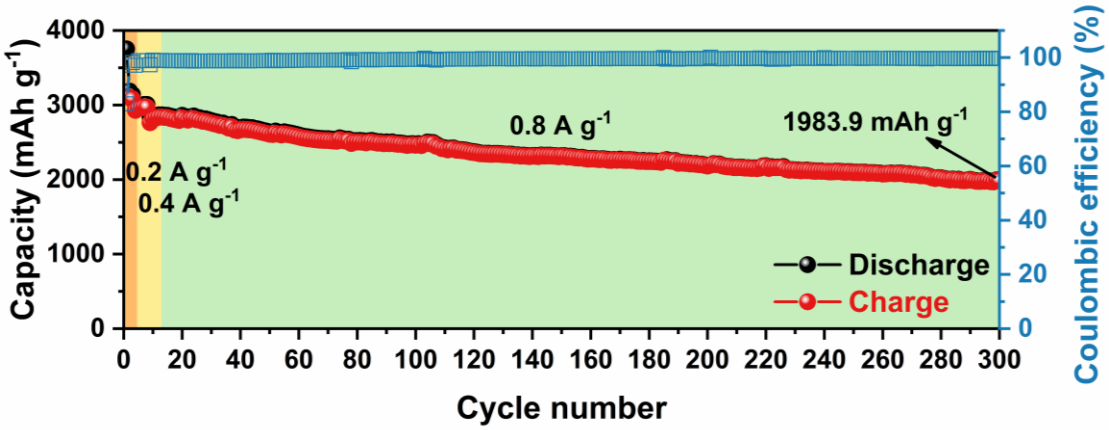

Fig. S20. Discharge/charge performance of SCNS-900 at 0.8 A g^{-1} (after activation by minor currents).

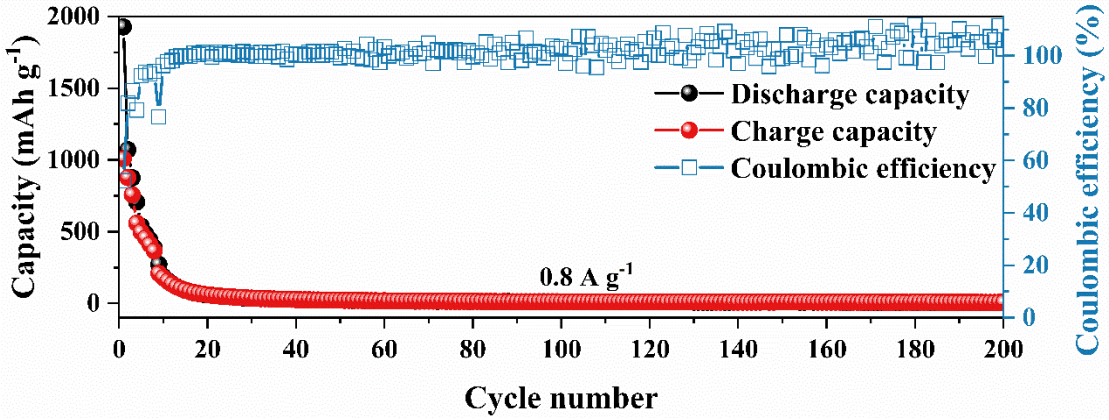

Fig. S21. Discharge/charge performance of Si-raw. The capacity of Si-raw shows a typical cliff-like decay before 20 cycles.

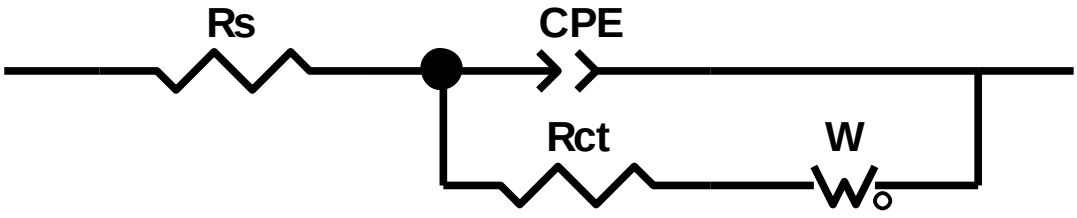

Fig. S22. Equivalent circuit diagram of the EIS for the samples. R_s is the intrinsic impedance, R_{ct} is the charge transfer resistance, CPE is the double layer capacitance, and W is the Warburg impedance.

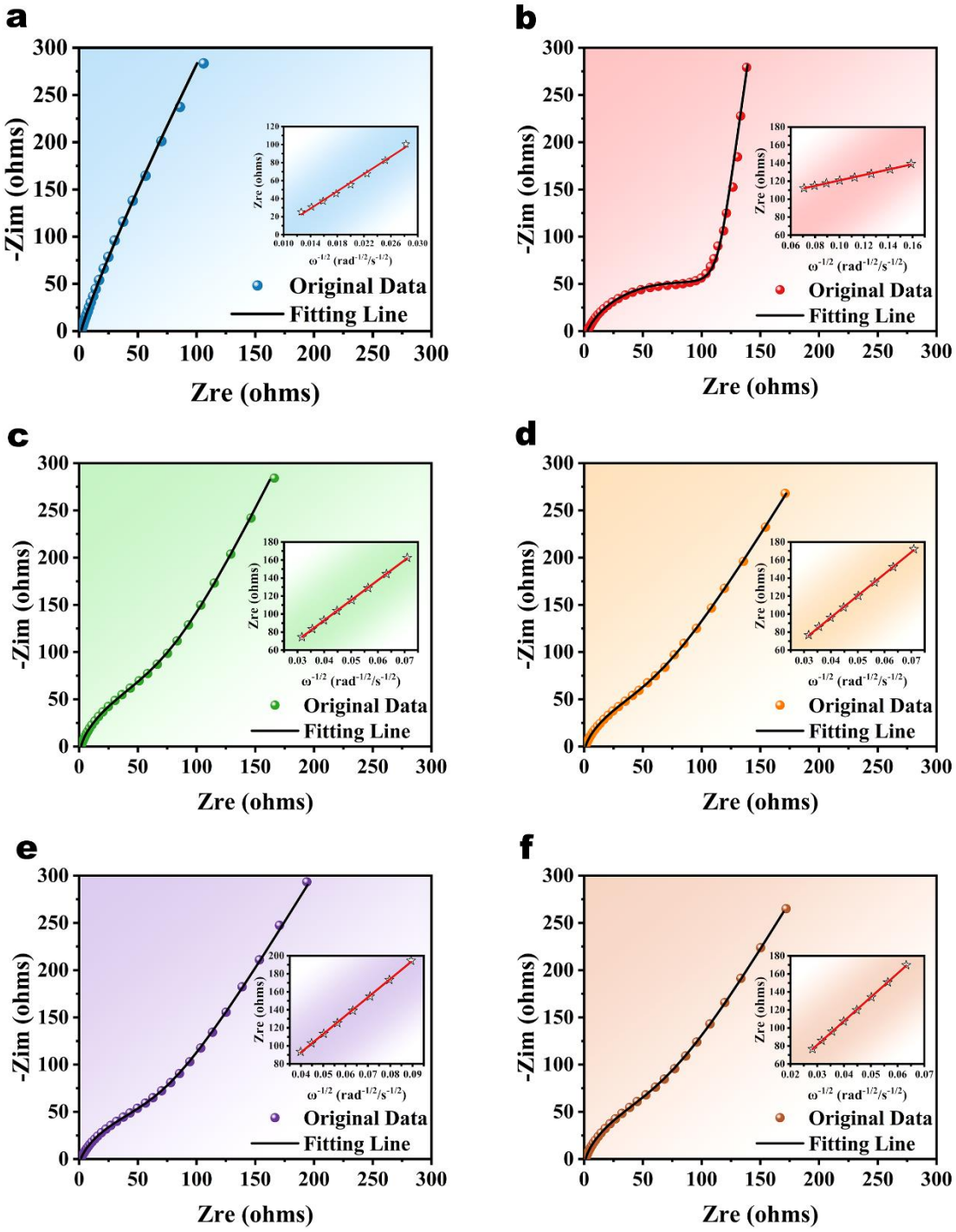

Fig. S23. EIS fitting results. a-f, EIS fits of SCNS (**a**), SCNS-800 (**b**), SCNS-900 (**c**), SCNS-1000 (**d**), SCNS-1100 (**e**), and SCNS-1200 (**f**) and their Zre-$\omega^{-1/2}$ fits of the Warburg section were applied to analyze the impedance of the system and to calculate the D_{Li+}. Obviously, the EIS of SCNS-900, SCNS-1000, SCNS-1100 and SCNS-1200 are relatively similar, while the impedance in the high-frequency region and the slope in the low-frequency region of SCNS-800 are both larger, implying that SCNS-800

(underdeveloped crystal) has a lot of internal contradictions. SCNS, on the other hand, has a very different EIS behavior from the others due to its high amorphous content, but in general the impedance and ion diffusion are not bad.

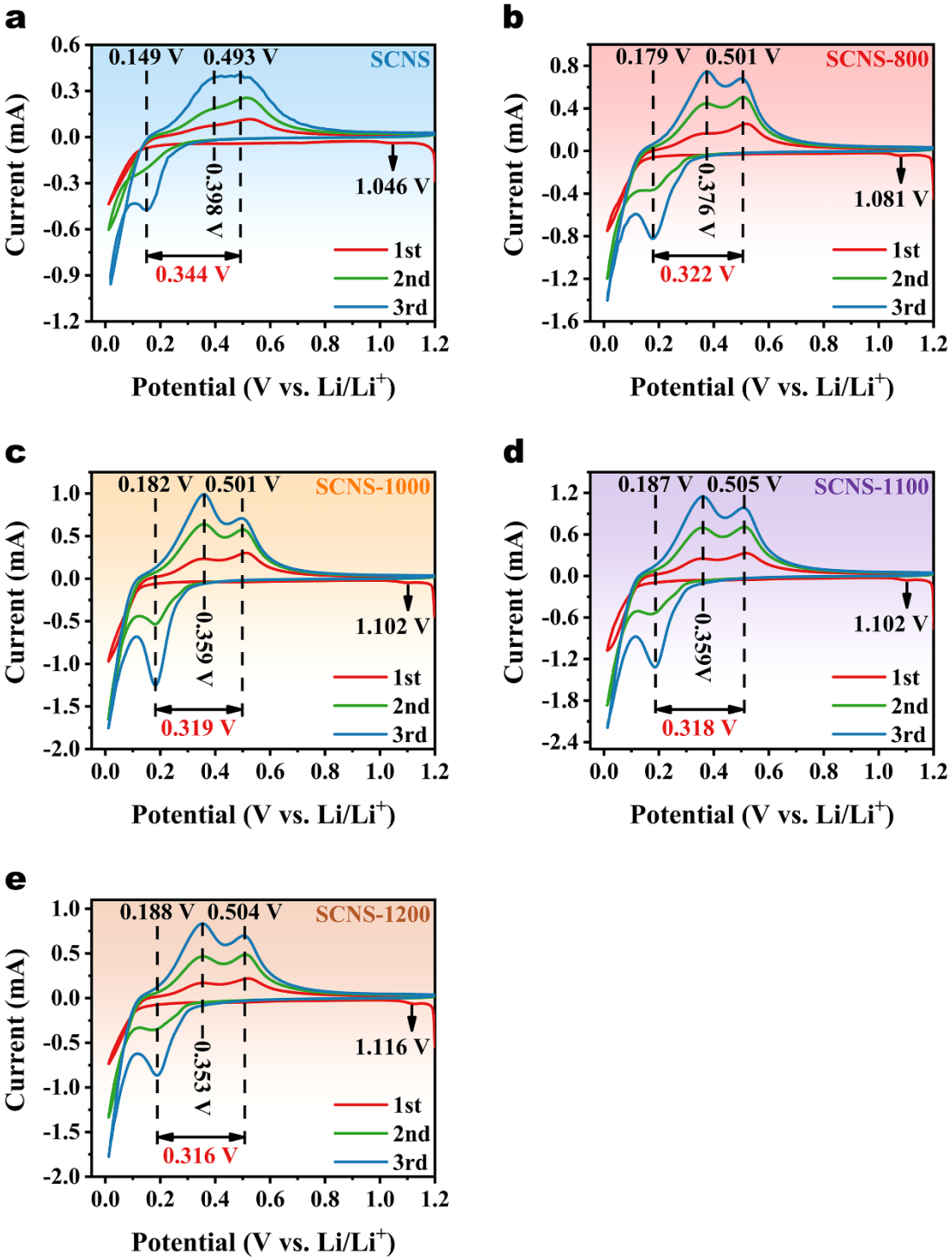

Fig. S24. CV curves. a-e, The lithiation/delithiation behaviours of SCNS (**a**), SCNS-800 (**b**),SCNS-1000 (**c**),SCNS-1100 (**d**) and SCNS-1200 (**e**) were characterized by CV. SCNS-800, SCNS-1000, SCNS-1100, and SCNS-1200 are apparently about the same

both in terms of side reactions at the first lithiation as well as lithiation and delithiation potentials, while SCNS is significantly different. The origin of this difference lies in the crystallographic properties of the two sides. SCNS has a high amorphous composition, reacts actively and delithiates easily. While with the improvement of crystallinity, the others present the phenomena of increasing side reaction and lithiation potential, decreasing first potential but increasing second potential of delithiation, and decreasing polarization between lithiation and delithiation. Thus, the perfection of the crystalline promotes the activity of the reaction somewhat, but mainly focuses on the conversion of Li-Si alloys. So the electrochemical activities between the amorphous and crystalline are essentially different.

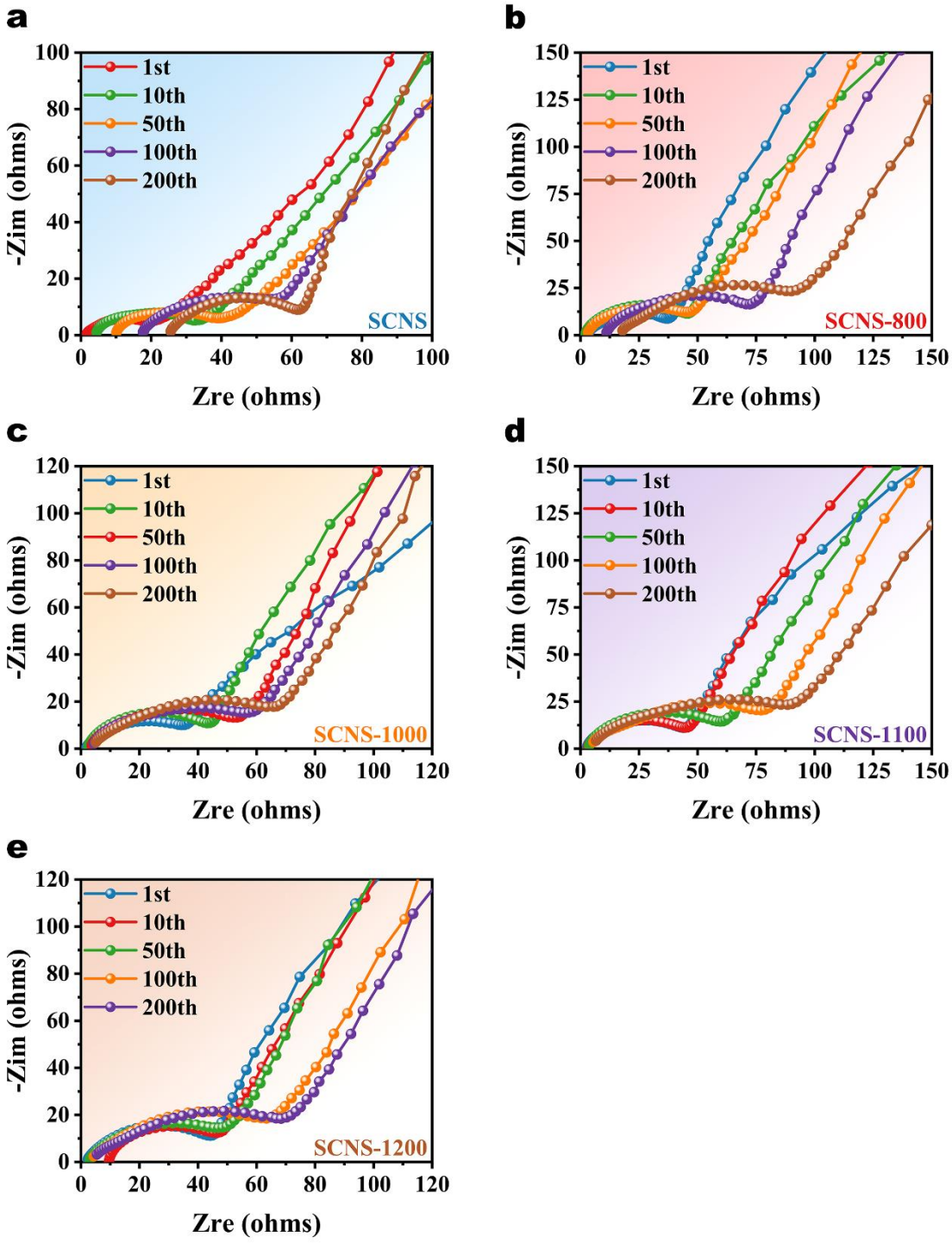

Fig. S25. EIS spectra after cycling. a-e, EIS spectra of SCNS (**a**), SCNS-800 (**b**), SCNS-1000 (**c**), SCNS-1100 (**d**) and SCNS-1200 (**e**) after the 1st, 10th, 50th, 100th and 200th cycles were used to analyze the impedance evolution during cycling. In fact, the capacity decay will be obviously reflected in the increase of impedance. The ohmic impedance of SCNS is clearly gradually increasing as shown in **a**, indicating that the cliff-like decay of its capacity is due to the destruction of the electrode macrostructure.

Whereas, SCNS-800 has both ohmic and charge transfer impedance increases, implying that both the macroscopic and microscopic structures of the electrode have collapsed. On the other hand, SCNS-1000, SCNS-1100 and SCNS-1200 have mainly the increase of charge transfer impedance, suggesting that the breakdown of the microstructure plays a dominant role in the capacity decay. Therefore, the impedance evolution is actually the variation of the electrode structure in essence.

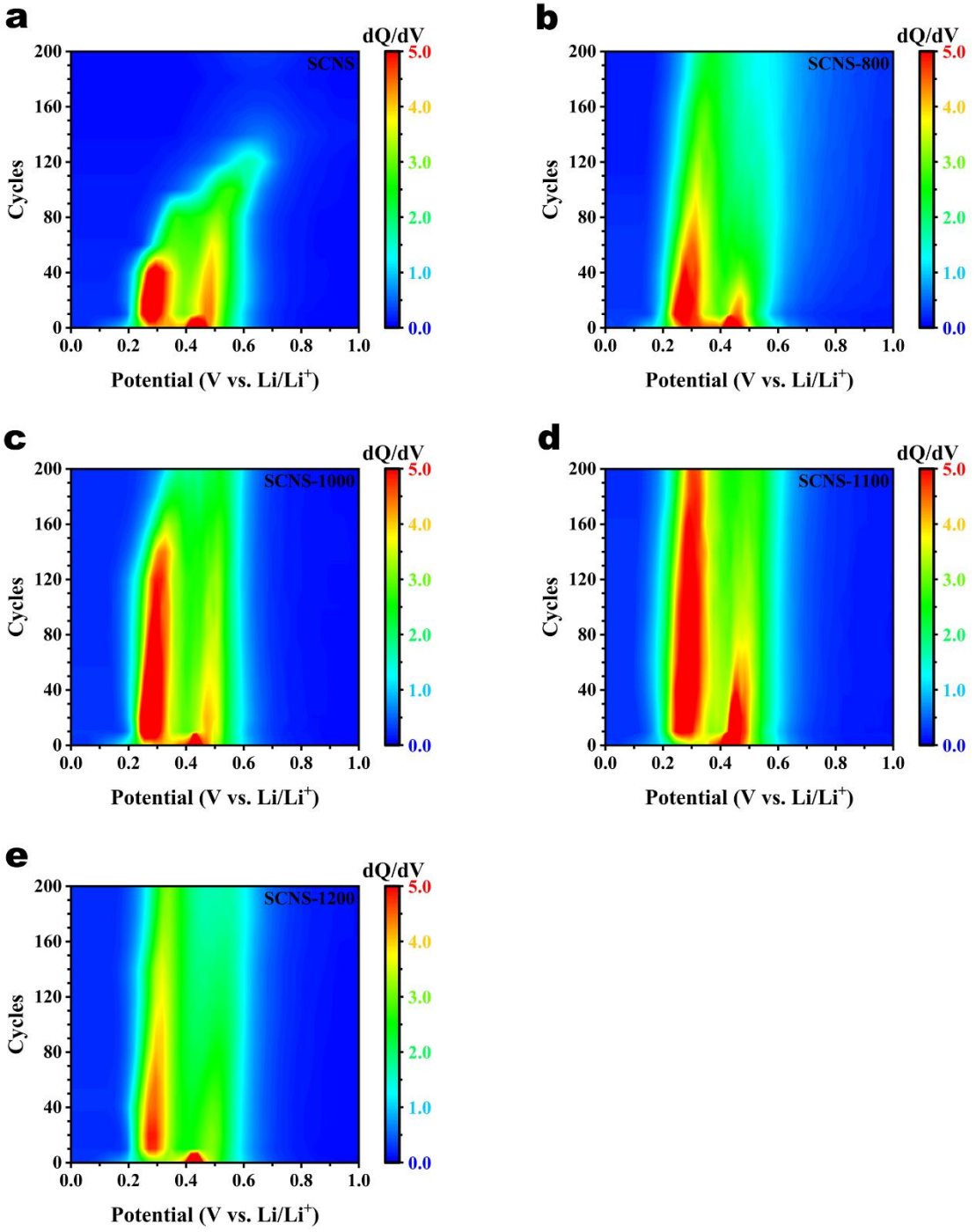

Fig. S26. Differential of reversible capacity to voltage (dQ/dV) waterfall diagram

of the samples with cycling. a-e, The dQ/dV waterfall diagrams of the SCNS (**a**), SCNS-800 (**b**), SCNS-1000 (**c**), SCNS-1100 (**d**) and SCNS-1200 (**e**) reversible (charging) processes were employed to visualize the electrochemical reaction windows and activities during their cycling. The attenuation of the electrochemical activity of SCNS is caused by the weakening of the Li-Si alloy conversion, which is reflected in **a** by the prior loss of the first potential of delithiation at around 0.3 V. The others are all due to the decline of the second potential (0.4-0.5 V) of delithiation resulting in the inability to fully delithiate Li^+, except for SCNS-1000 which is also accompanied by a gradual weakening of the first potential after 120 cycles. These behaviors depend on the crystal phase and the stability of the structure, which also determines the electrochemical window.

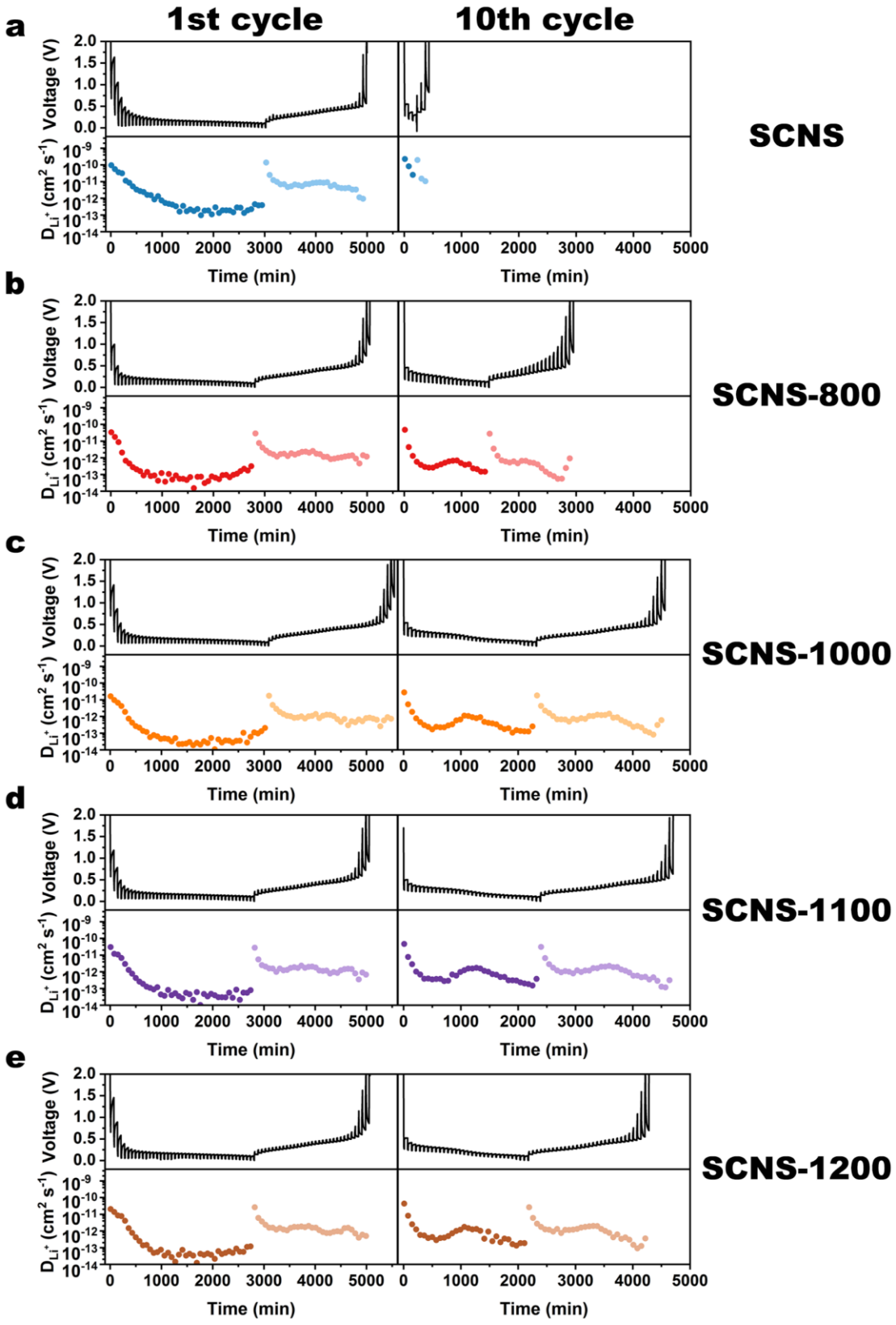

Fig. S27. Galvanostatic intermittent titration technique (GITT) analysis of the cells for the samples. a-e, The dynamic voltage and calculated lithium diffusion (D_{Li+}) presented for SCNS (**a**), SCNS-800 (**b**), SCNS-1000 (**c**), SCNS-1100 (**d**), and SCNS-

1200 (**e**) at the 1st and 10th cycles in the GITT test.

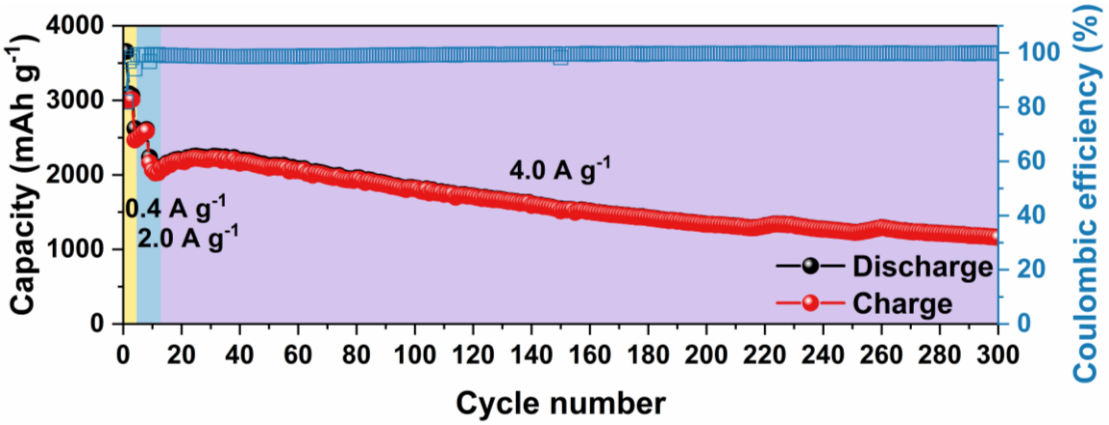

Fig. S28. Discharge/charge performance of SCNS-900 at 4.0 A g^{-1} (after activation by minor currents).

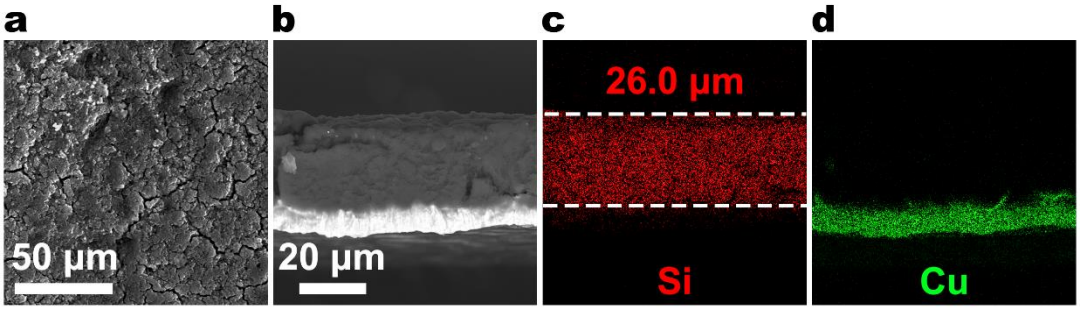

Fig. S29. SEM of the SCNS-900 electrode after 300 cycles. a, SEM of the electrode surface. **b-d,** SEM of the electrode cross-section (**b**), and the corresponding mapping of Si (**c**) and Cu (**d**).

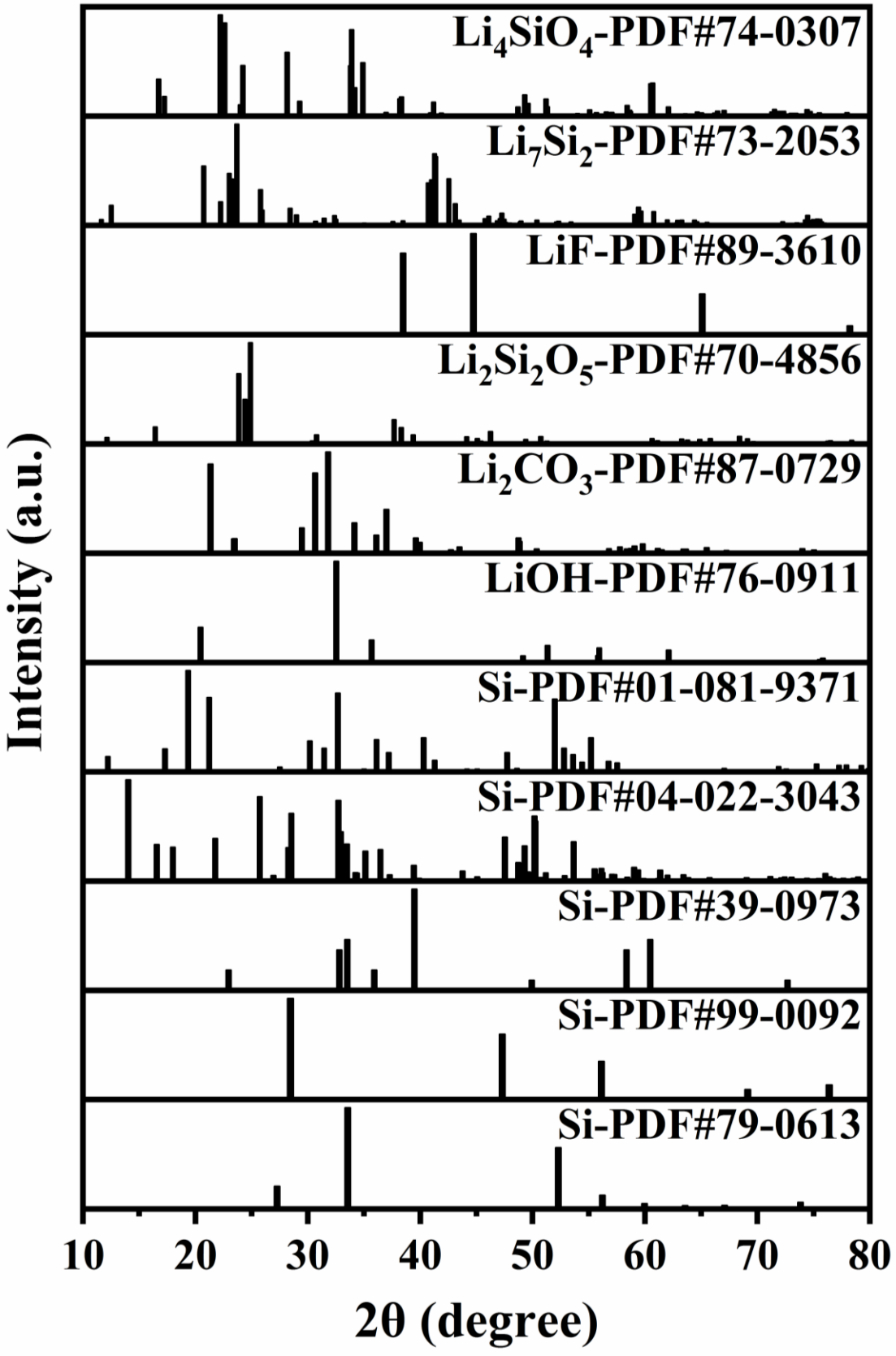

Fig. S30. Standard powder diffraction file (PDF) of the phases present in the XRD characterization of the manuscript.

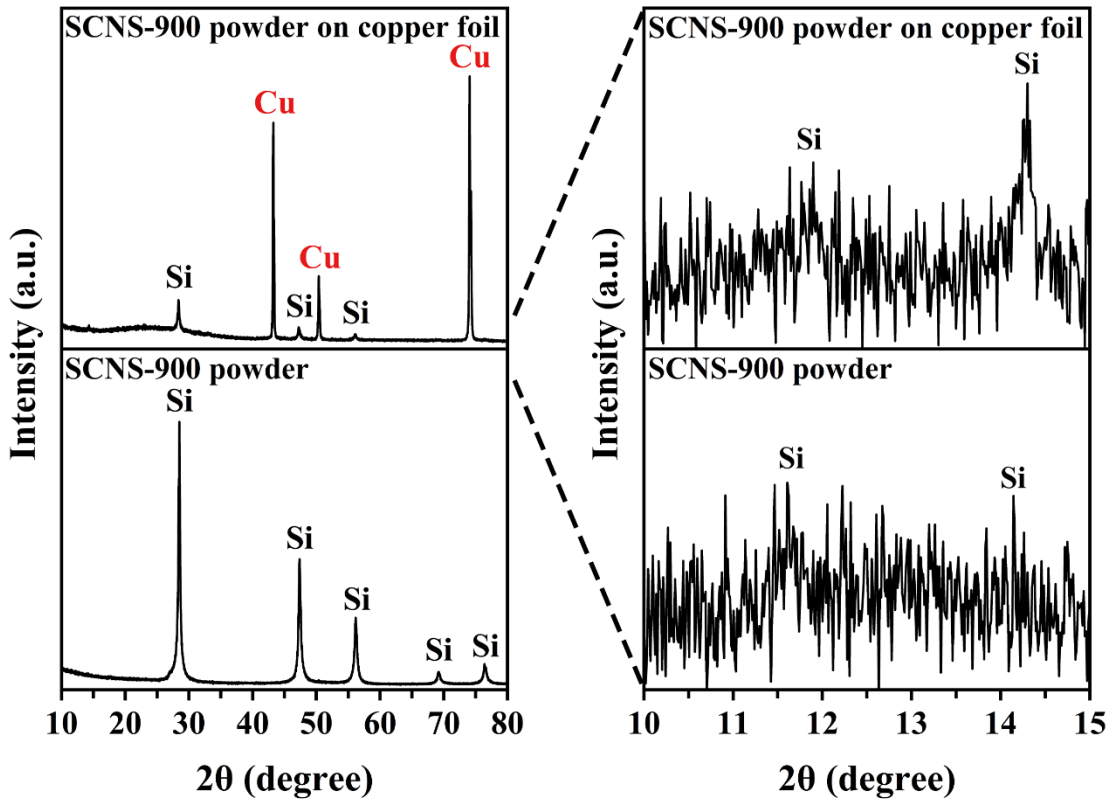

Fig. S31. XRD spectra (at 2° min^{-1}) of the SCNS-900 powder before and after attachment to copper foil. Apparently, the existence of the Cu foil, although weakening the characteristic strong peaks of Si, enhances the weak peaks at 10-15°, which is attributed to the special crystal structure of SCNS-900 as well as to the interaction of the Cu foil with the Cu K_{α}-ray.

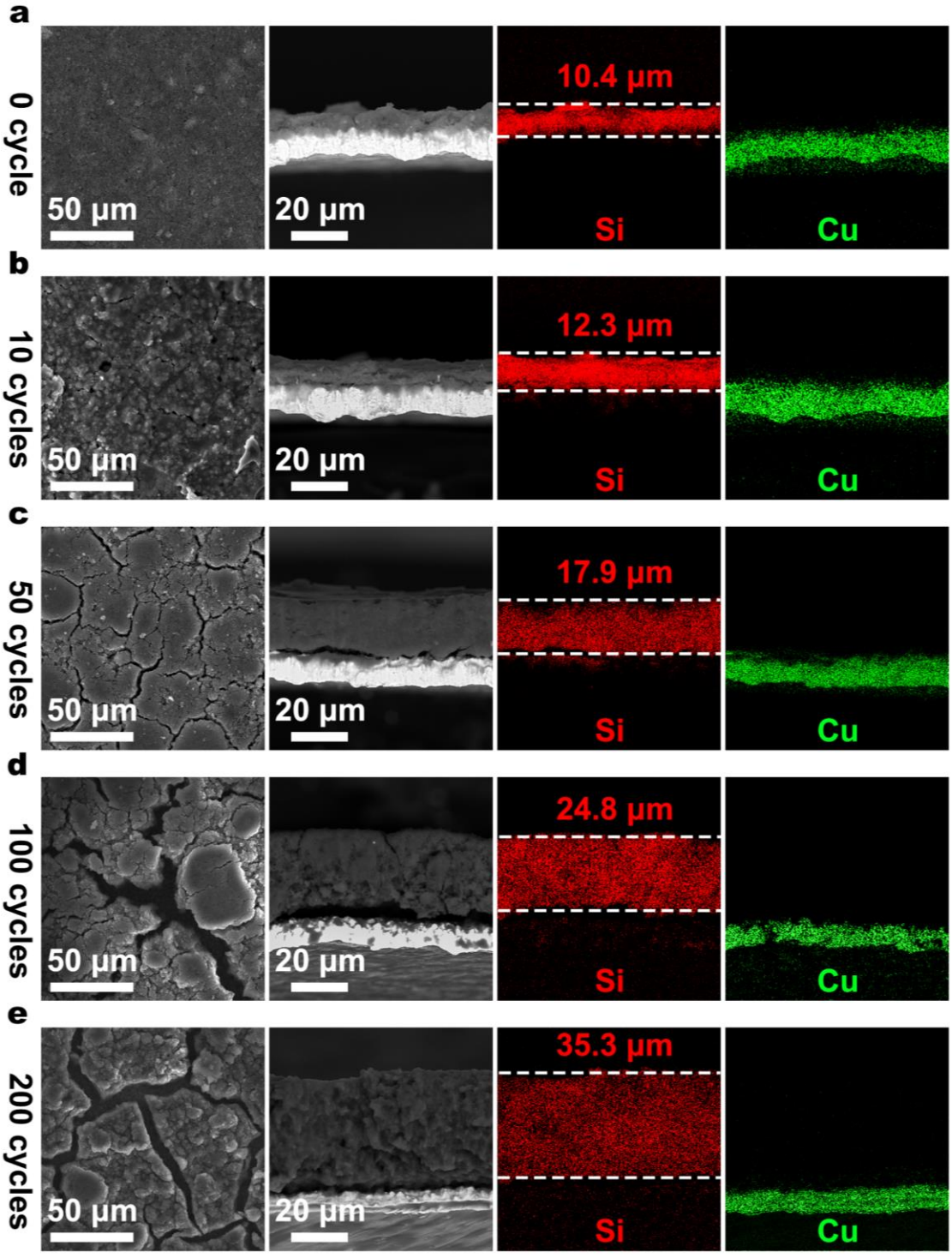

Fig. S32. SEM of the SCNS electrodes before and after cycling. a-e, SEM images of the surface and cross-section as well as the corresponding Si and Cu mapping of the cross-section after 0 (**a**), 10 (**b**), 50 (**c**), 100 (**d**) and 200 (**e**) cycles of the electrodes, respectively.

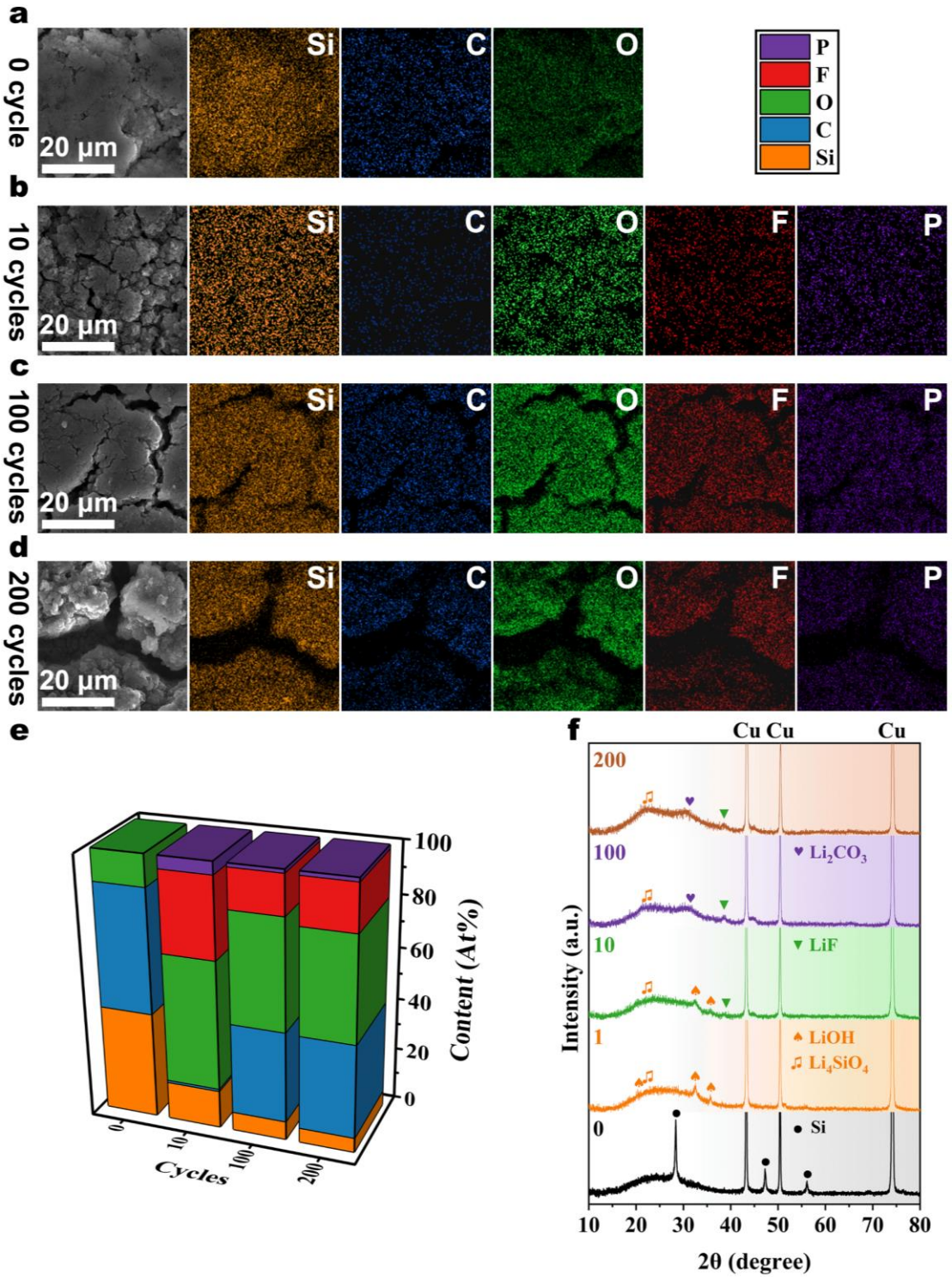

Fig. S33. Composition of the SCNS electrodes before and after cycling. a-d, SEM images of the surface and their corresponding elemental mapping after 0 (**a**), 10 (**b**), 100 (**c**) and 200 (**d**) cycles of the electrodes, respectively. **e,** The relative atomic contents of Si, C, O, F and P in the electrodes before and after cycling as obtained by EDS attached to the SEM. **f,** Slow-scan (2 ° min^{-1}) XRD spectra of the electrodes after 0, 1, 10, 100 and 200 cycles.

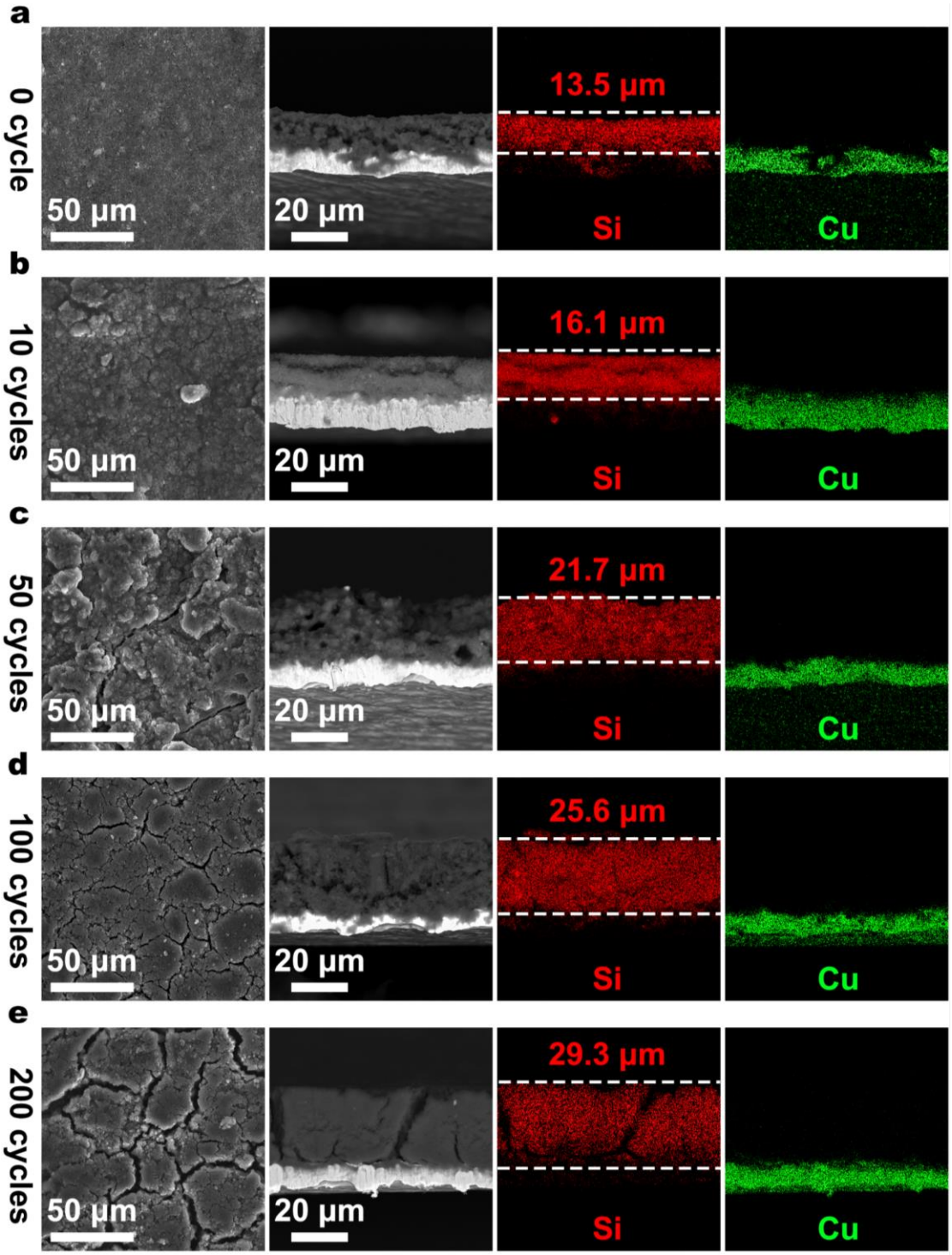

Fig. S34. SEM of the SCNS-800 electrodes before and after cycling. a-e, SEM images of the surface and cross-section as well as the corresponding Si and Cu mapping of the cross-section after 0 (**a**), 10 (**b**), 50 (**c**), 100 (**d**) and 200 (**e**) cycles of the electrodes, respectively.

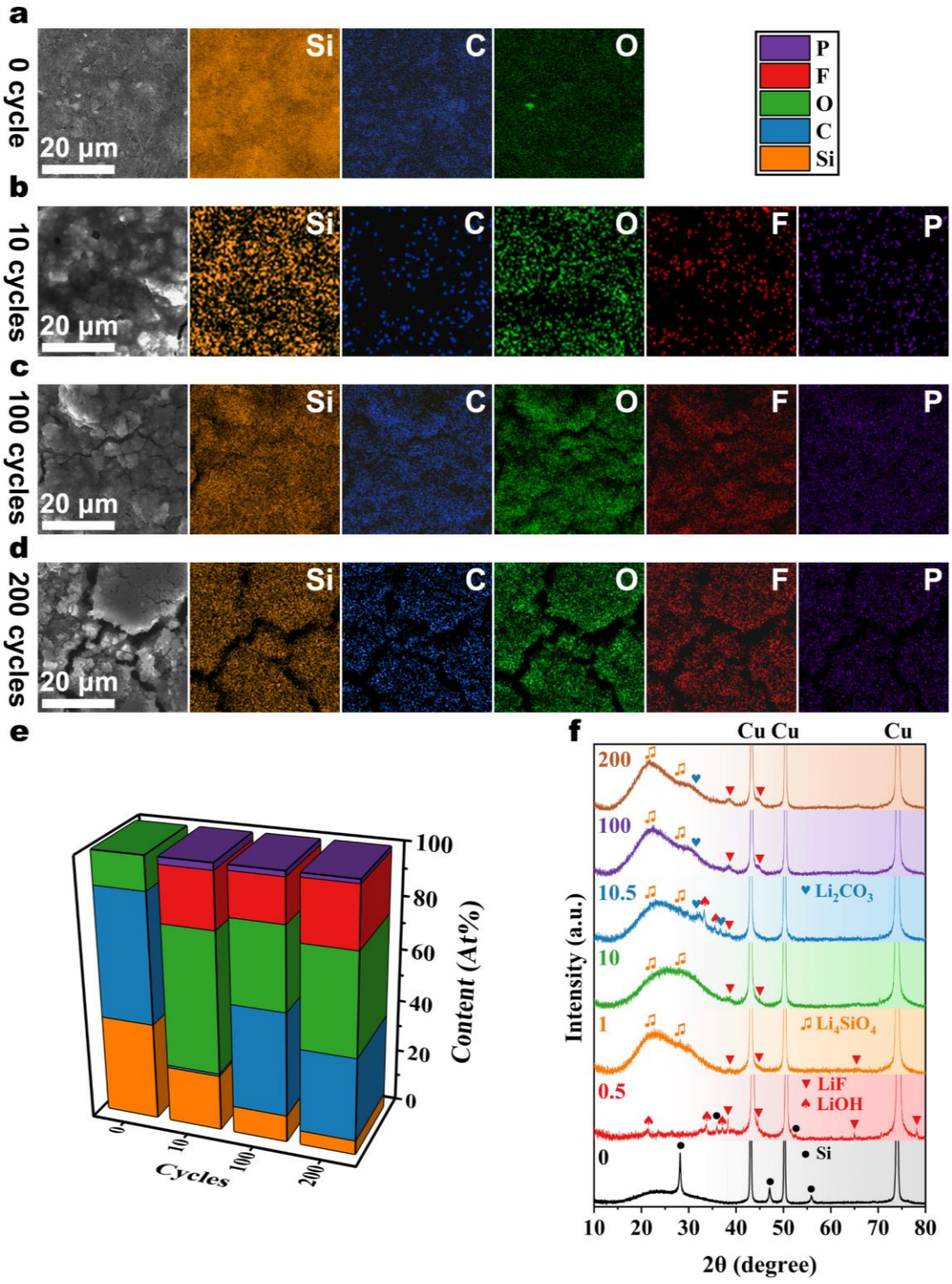

Fig. S35. Composition of the SCNS-800 electrodes before and after cycling. a-d, SEM images of the surface and their corresponding elemental mapping after 0 (**a**), 10 (**b**), 100 (**c**) and 200 (**d**) cycles of the electrodes, respectively. **e,** The relative atomic contents of Si, C, O, F and P in the electrodes before and after cycling as obtained by EDS attached to the SEM. **f,** Slow-scan (2 ° min^{-1}) XRD spectra of the electrodes after 0, 0.5, 1, 10, 10.5, 100 and 200 cycles.

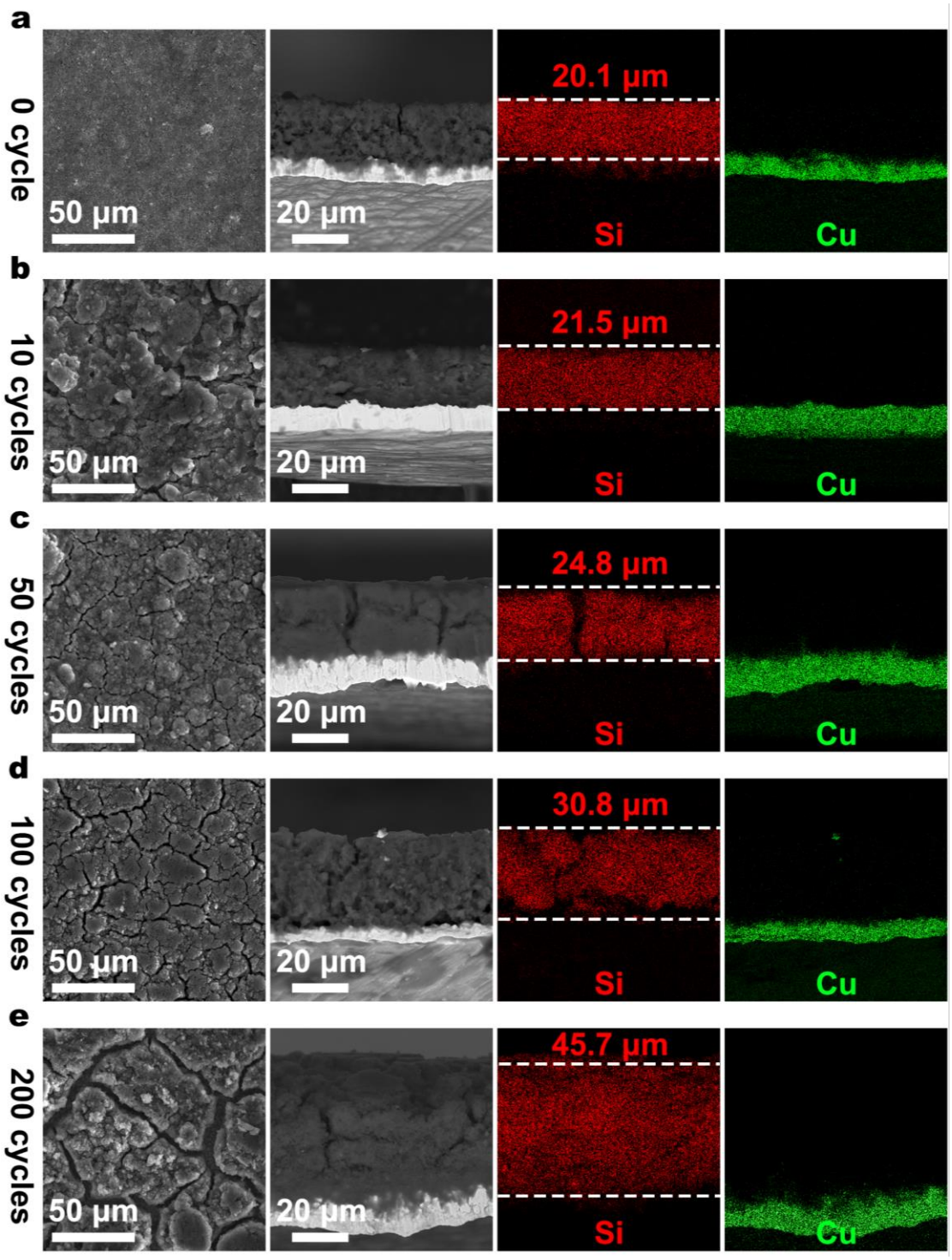

Fig. S36. SEM of the SCNS-1000 electrodes before and after cycling. a-e, SEM images of the surface and cross-section as well as the corresponding Si and Cu mapping of the cross-section after 0 (**a**), 10 (**b**), 50 (**c**), 100 (**d**) and 200 (**e**) cycles of the electrodes, respectively.

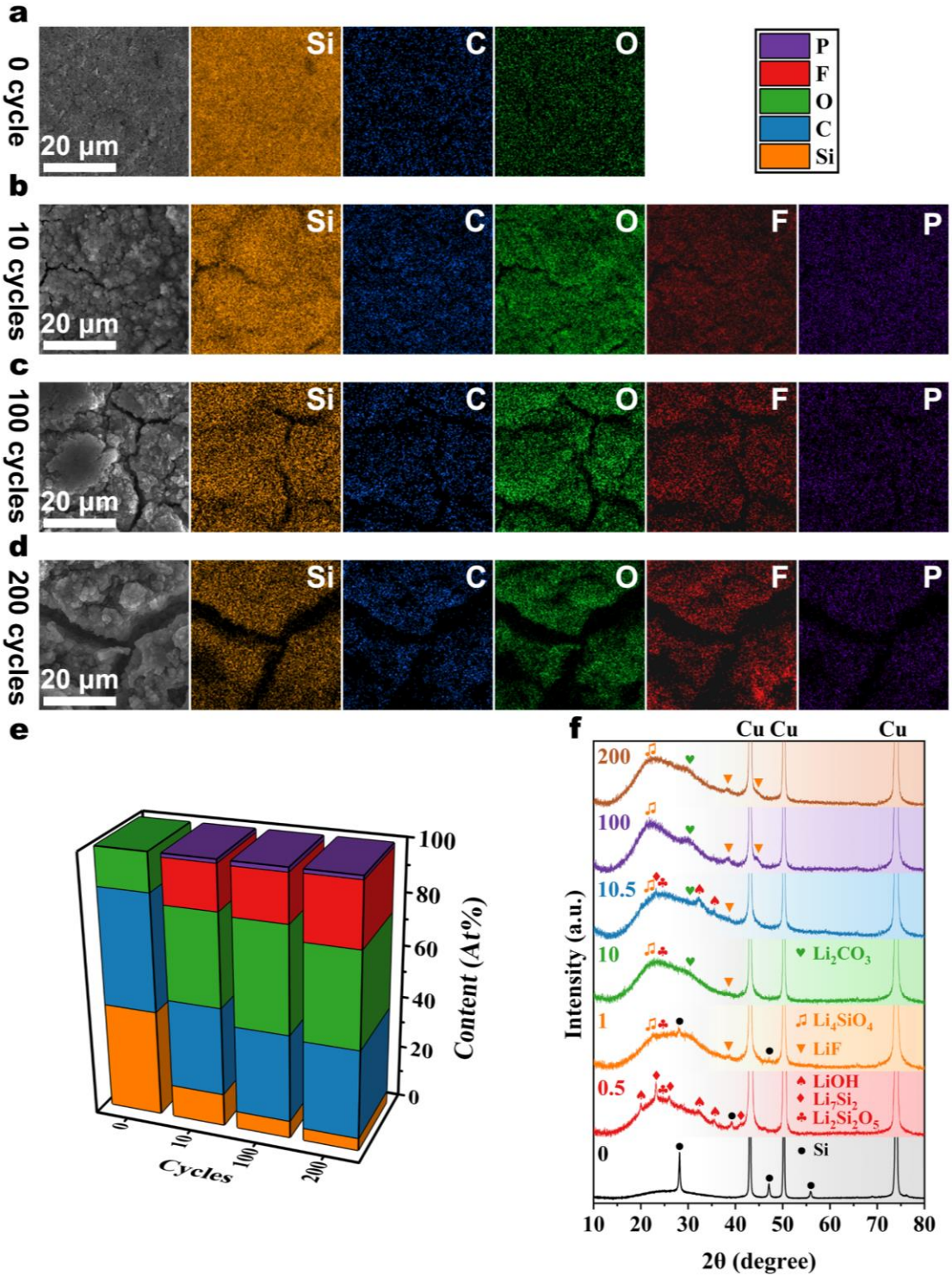

Fig. S37. Composition of the SCNS-1000 electrodes before and after cycling. a-d, SEM images of the surface and their corresponding elemental mapping after 0 (**a**), 10 (**b**), 100 (**c**) and 200 (**d**) cycles of the electrodes, respectively. **e,** The relative atomic contents of Si, C, O, F and P in the electrodes before and after cycling as obtained by EDS attached to the SEM. **f,** Slow-scan (2 ° min^{-1}) XRD spectra of the electrodes after 0, 0.5, 1, 10, 10.5, 100 and 200 cycles.

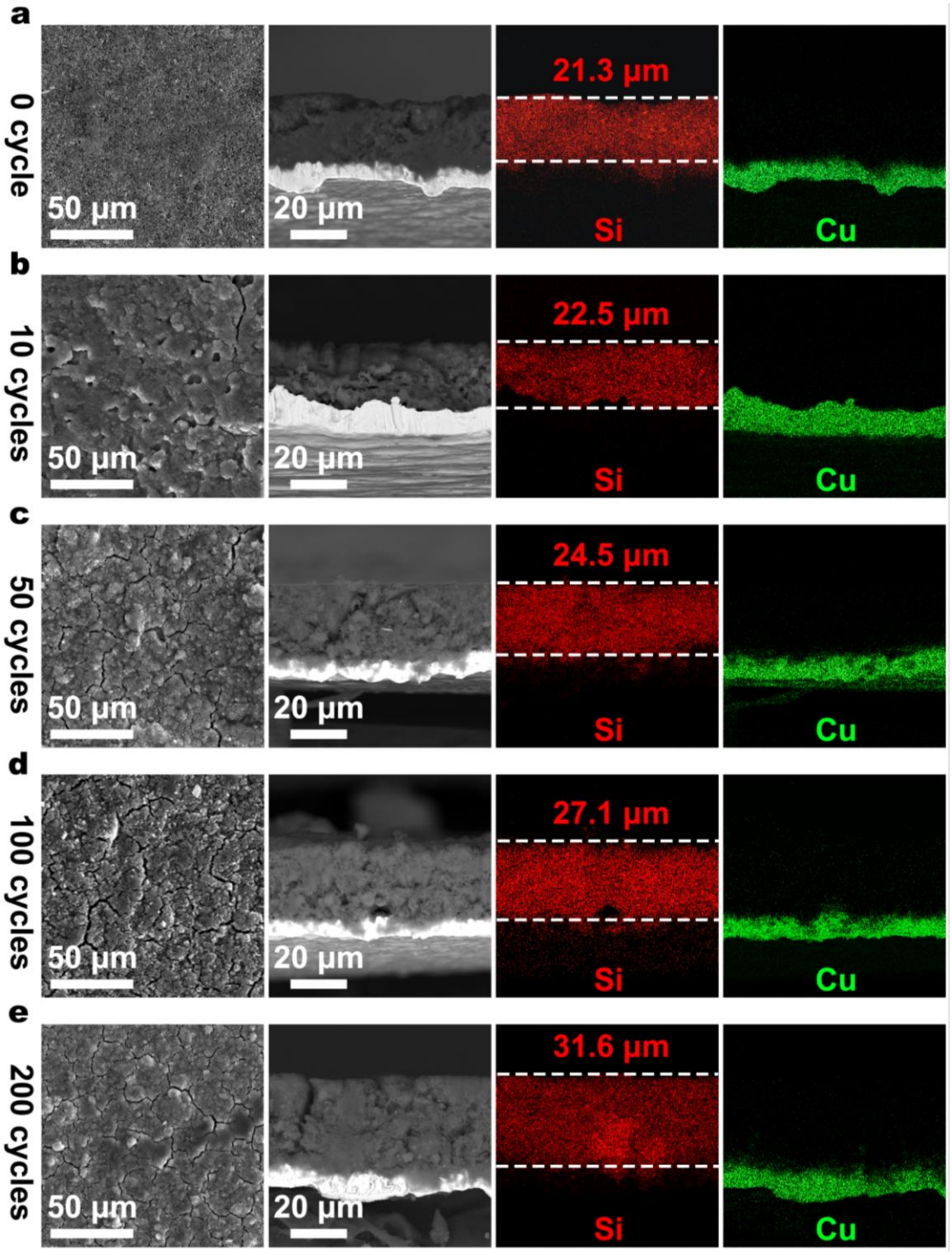

Fig. S38. SEM of the SCNS-1100 electrodes before and after cycling. a-e, SEM images of the surface and cross-section as well as the corresponding Si and Cu mapping of the cross-section after 0 (**a**), 10 (**b**), 50 (**c**), 100 (**d**) and 200 (**e**) cycles of the electrodes, respectively.

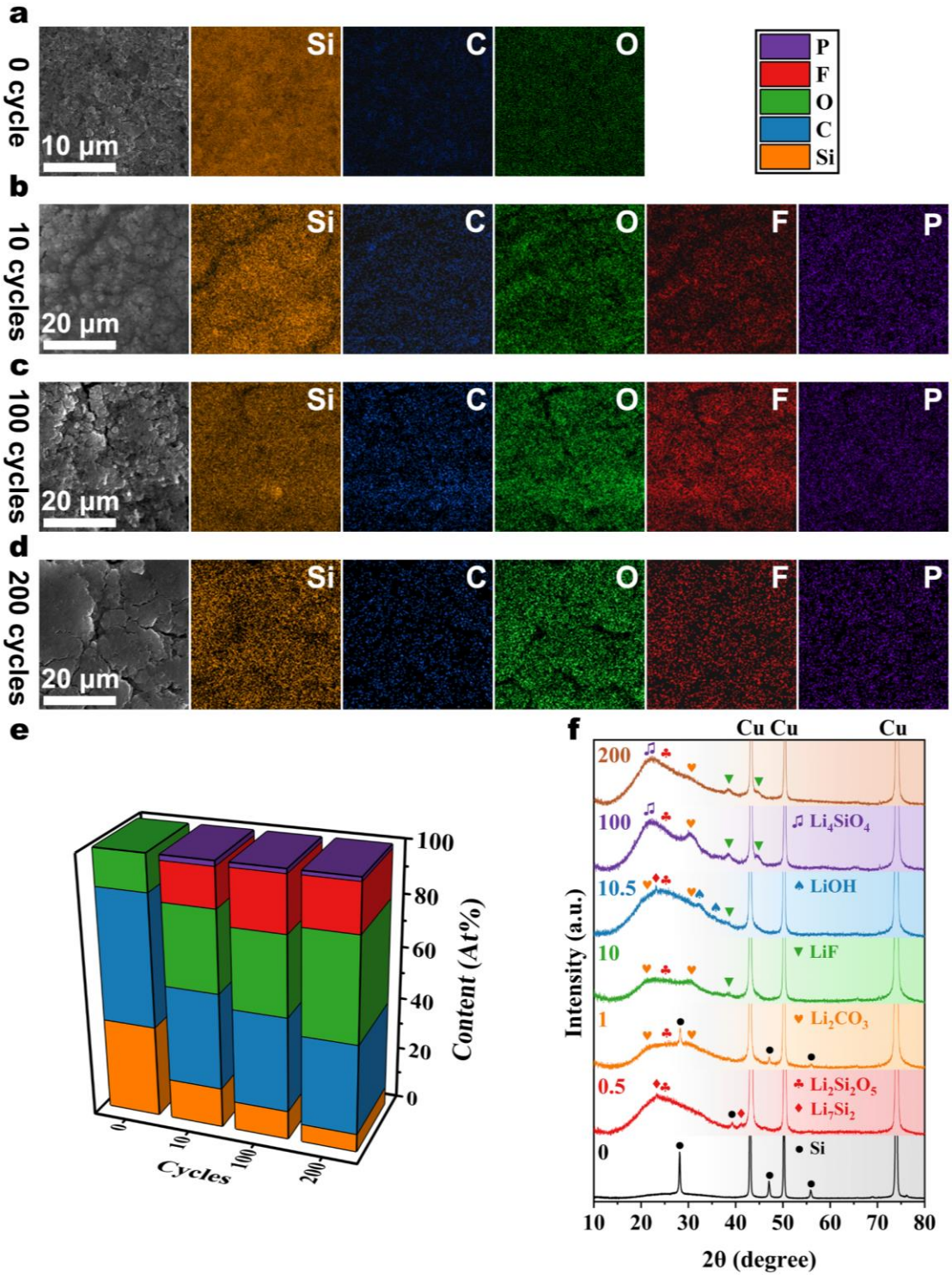

Fig. S39. Composition of the SCNS-1100 electrodes before and after cycling. a-d, SEM images of the surface and their corresponding elemental mapping after 0 (**a**), 10 (**b**), 100 (**c**) and 200 (**d**) cycles of the electrodes, respectively. **e,** The relative atomic contents of Si, C, O, F and P in the electrodes before and after cycling as obtained by EDS attached to the SEM. **f,** Slow-scan (2 ° min^{-1}) XRD spectra of the electrodes after 0, 0.5, 1, 10, 10.5, 100 and 200 cycles.

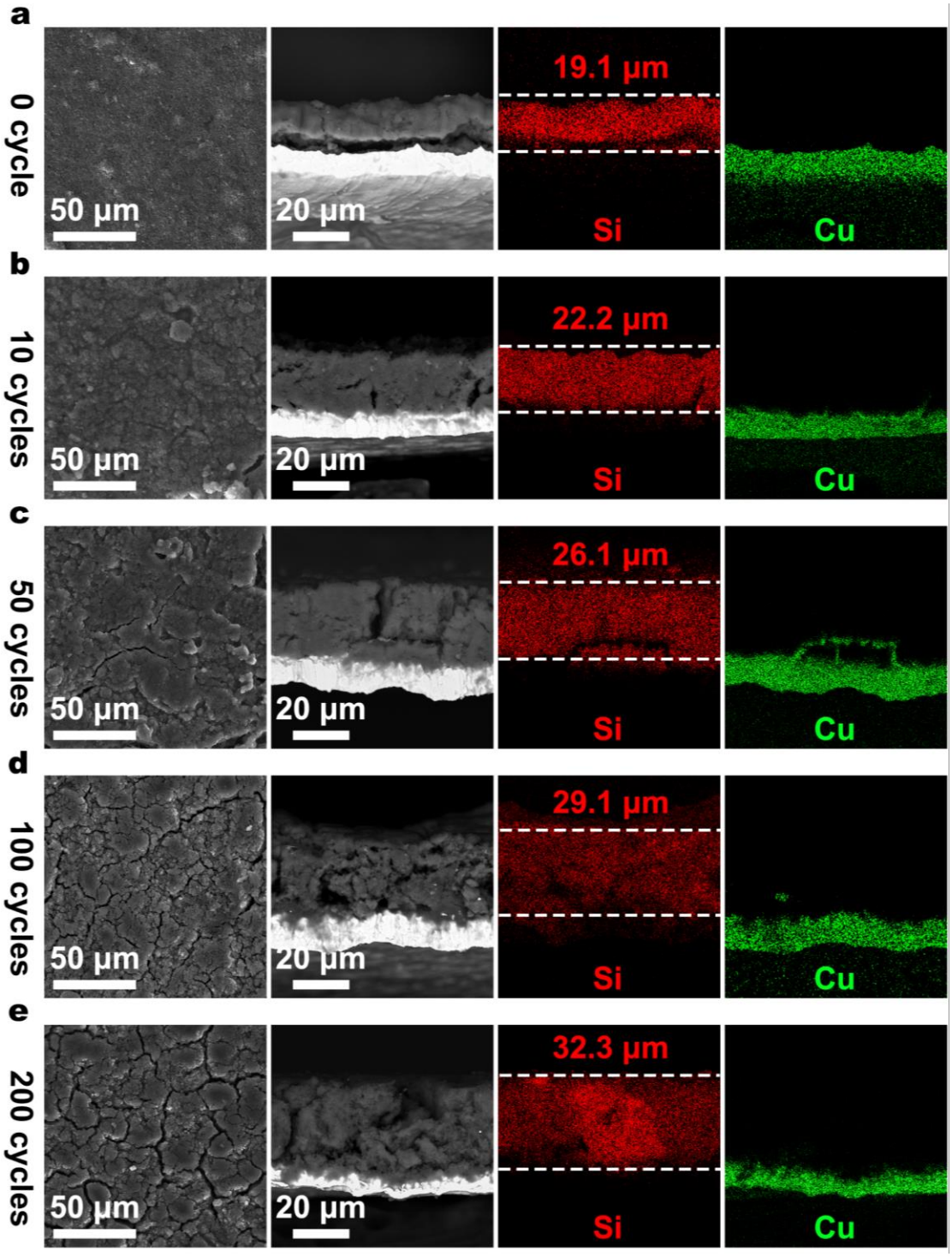

Fig. S40. SEM of the SCNS-1200 electrodes before and after cycling. a-e, SEM images of the surface and cross-section as well as the corresponding Si and Cu mapping of the cross-section after 0 (**a**), 10 (**b**), 50 (**c**), 100 (**d**) and 200 (**e**) cycles of the electrodes, respectively.

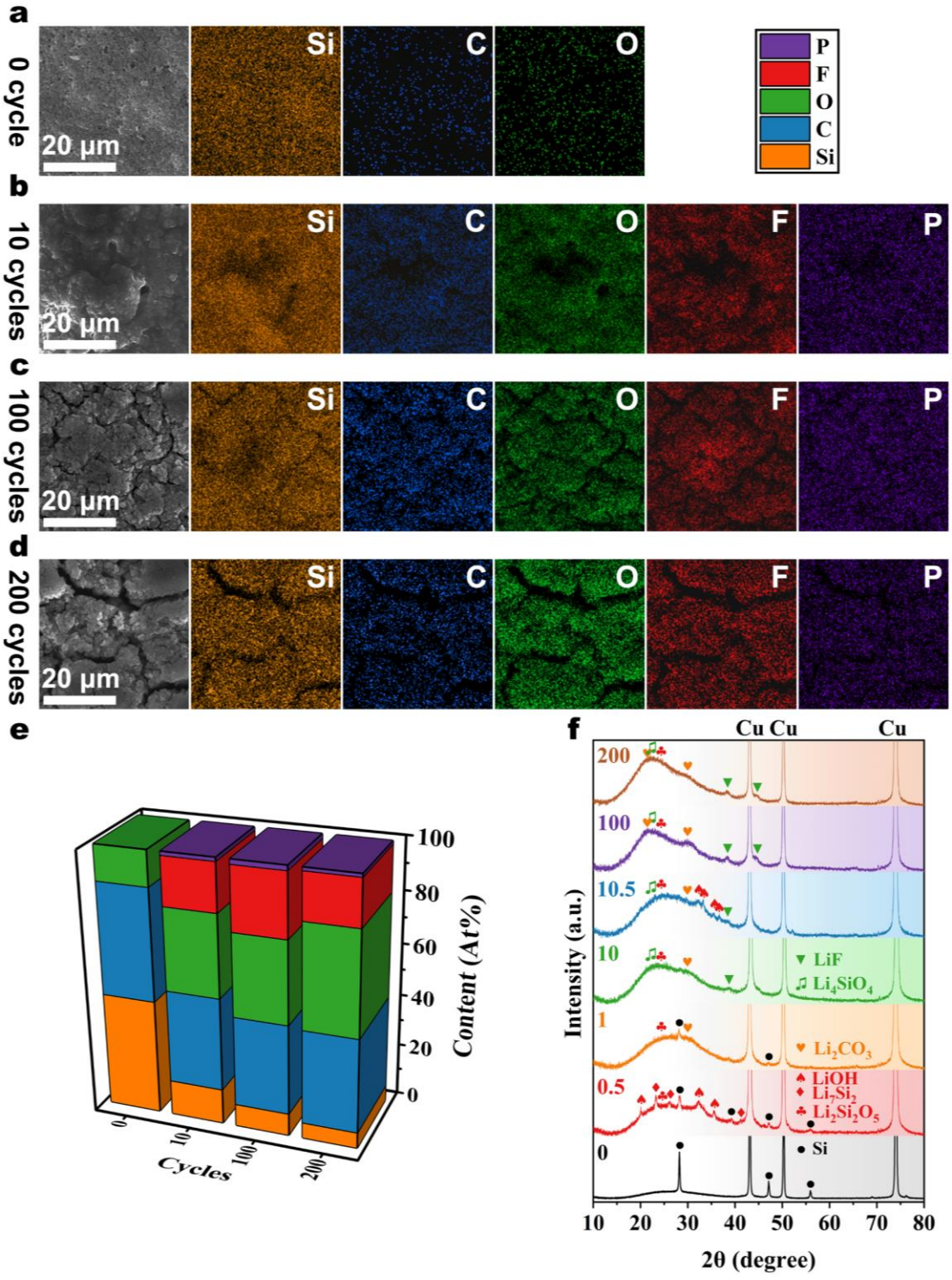

Fig. S41. Composition of the SCNS-1200 electrodes before and after cycling. a-d, SEM images of the surface and their corresponding elemental mapping after 0 (**a**), 10 (**b**), 100 (**c**) and 200 (**d**) cycles of the electrodes, respectively. **e,** The relative atomic contents of Si, C, O, F and P in the electrodes before and after cycling as obtained by EDS attached to the SEM. **f,** Slow-scan (2 ° min^{-1}) XRD spectra of the electrodes after 0, 0.5, 1, 10, 10.5, 100 and 200 cycles.

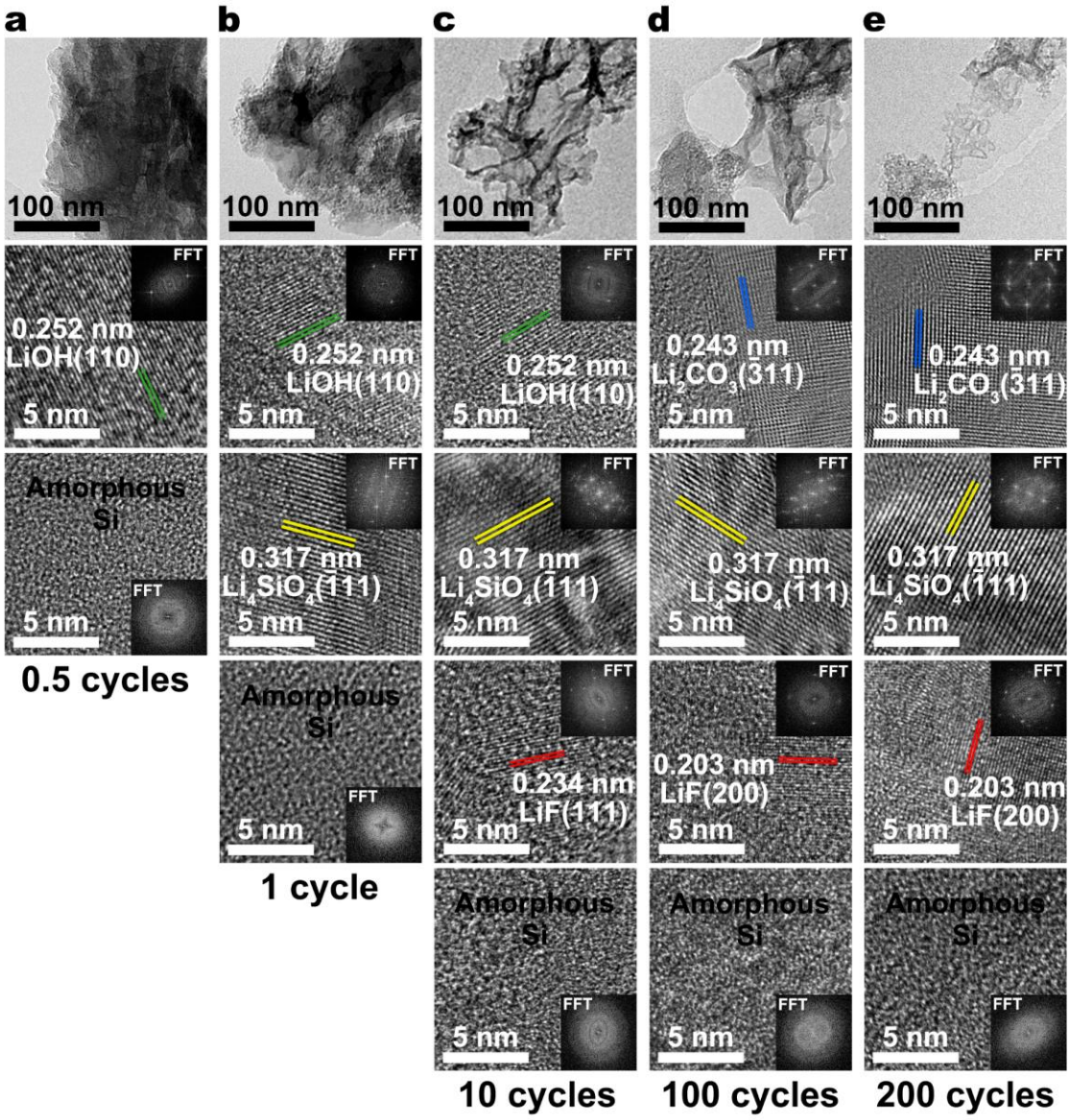

Fig. S42. AC-TEM characterization of SCNS after cycling. a-e, The morphology, composition and structure of SCNS were characterized at the ultramicro level by TEM and HRTEM (with FFT) after 0.5 (**a**), 1 (**b**), 10 (**c**), 100 (**d**) and 200 (**e**) cycles, respectively. In particular, the crystallographic composition and evolution of the solid electrolyte interface (SEI) and Si phase were observed with emphasis to figure out the correlation between the two and the electrochemical performance of SCNS.

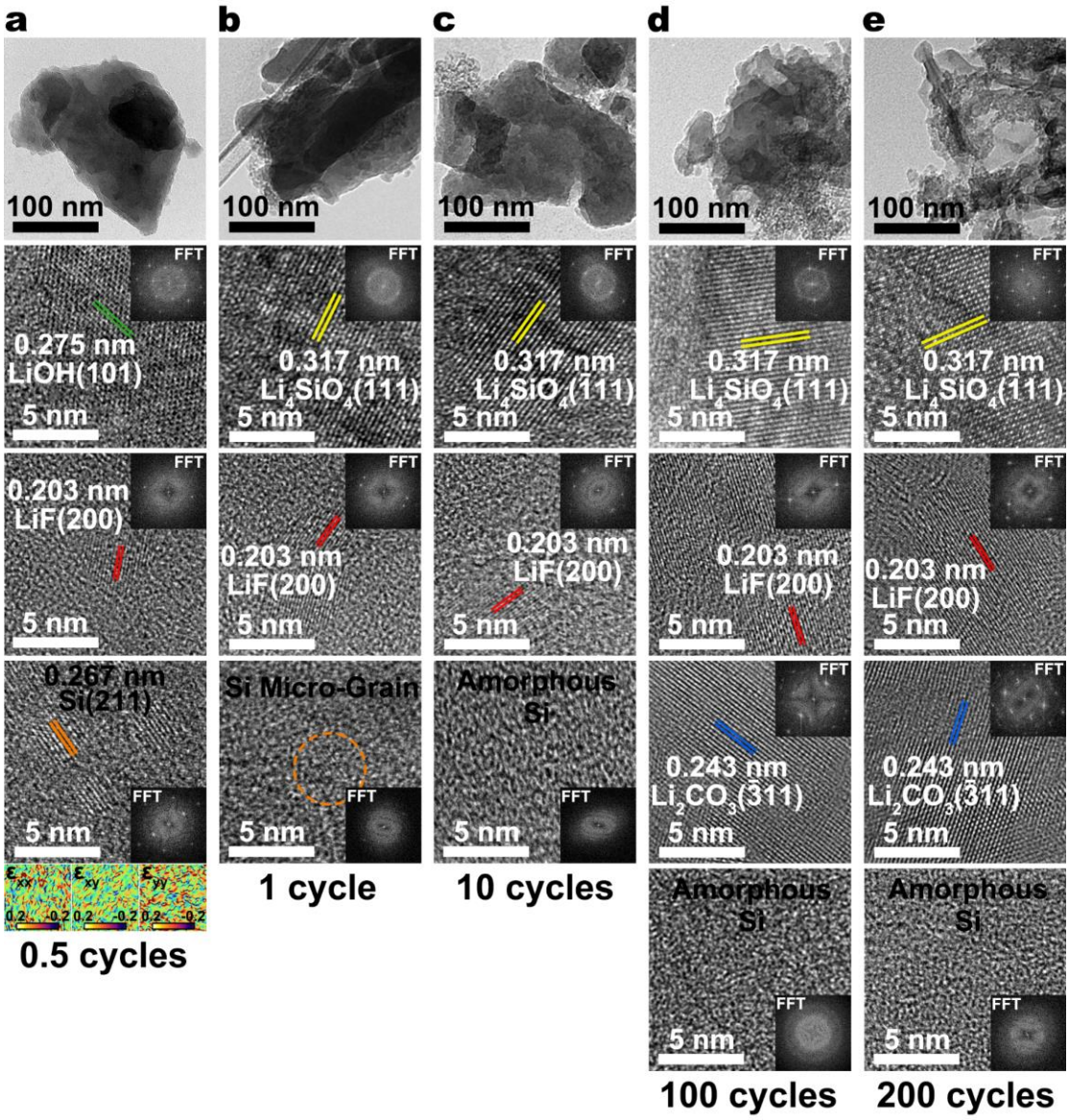

Fig. S43. AC-TEM characterization of SCNS-800 after cycling. a-e, The morphology, composition and structure of SCNS-800 were characterized at the ultramicro level by TEM and HRTEM (with FFT) after 0.5 (**a**), 1 (**b**), 10 (**c**), 100 (**d**) and 200 (**e**) cycles, respectively. In particular, the crystallographic composition and evolution of the SEI and Si phase were observed with emphasis to figure out the correlation between the two and the electrochemical performance of SCNS-800. In addition, the ε_{xx}, ε_{xy} and ε_{yy} microstrain distributions of the HRTEM with crystalline Si were visualized by the GPA method to observe the pinning solidity of the crystalline phases in order to determine the cyclic mechanical properties of SCNS-800.

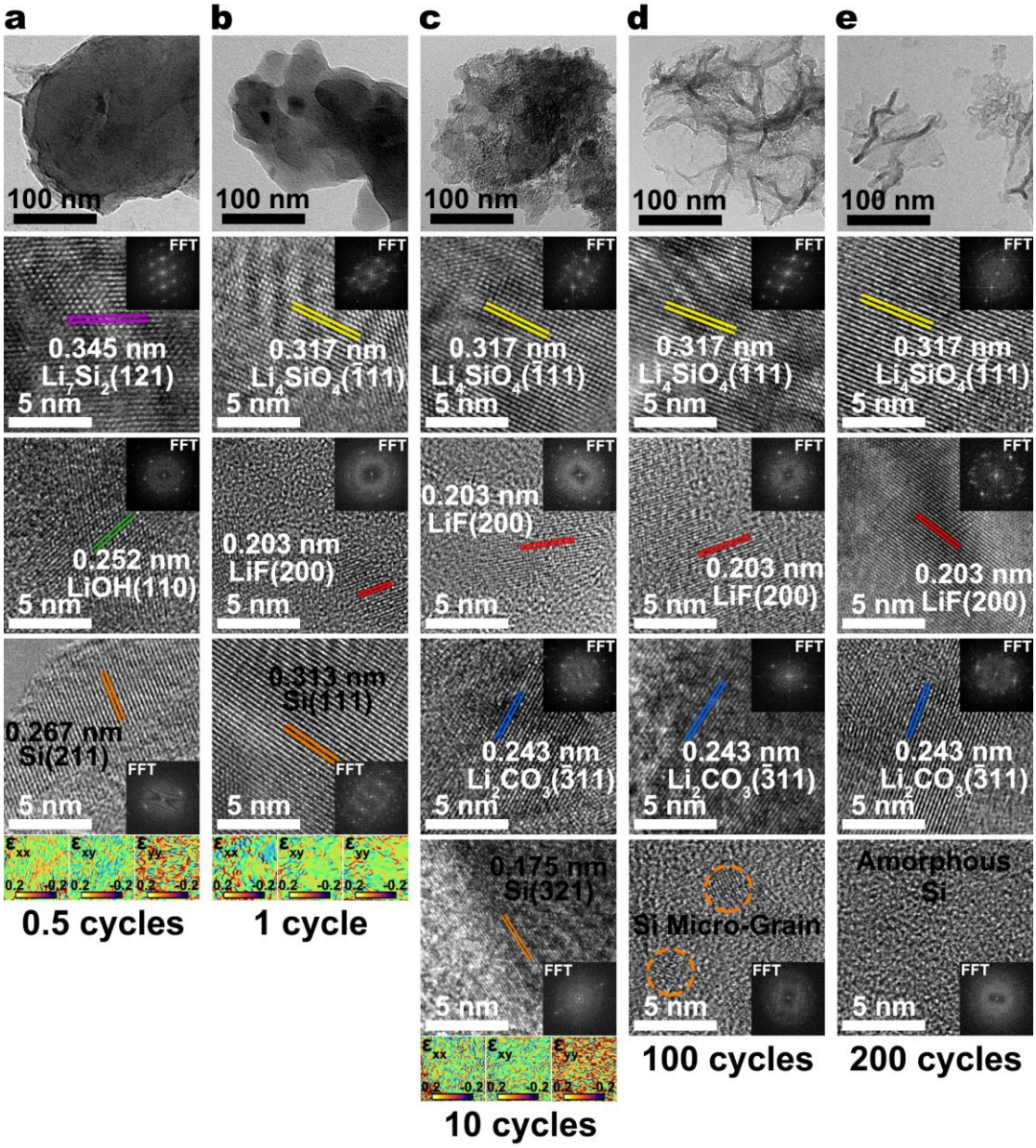

Fig. S44. AC-TEM characterization of SCNS-1000 after cycling. a-e, The morphology, composition and structure of SCNS-1000 were characterized at the ultramicro level by TEM and HRTEM (with FFT) after 0.5 (**a**), 1 (**b**), 10 (**c**), 100 (**d**) and 200 (**e**) cycles, respectively. In particular, the crystallographic composition and evolution of the SEI and Si phase were observed with emphasis to figure out the correlation between the two and the electrochemical performance of SCNS-1000. In addition, the ε_{xx}, ε_{xy} and ε_{yy} microstrain distributions of the HRTEM with crystalline Si were visualized by the GPA method to observe the pinning solidity of the crystalline phases in order to determine the cyclic mechanical properties of SCNS-1000.

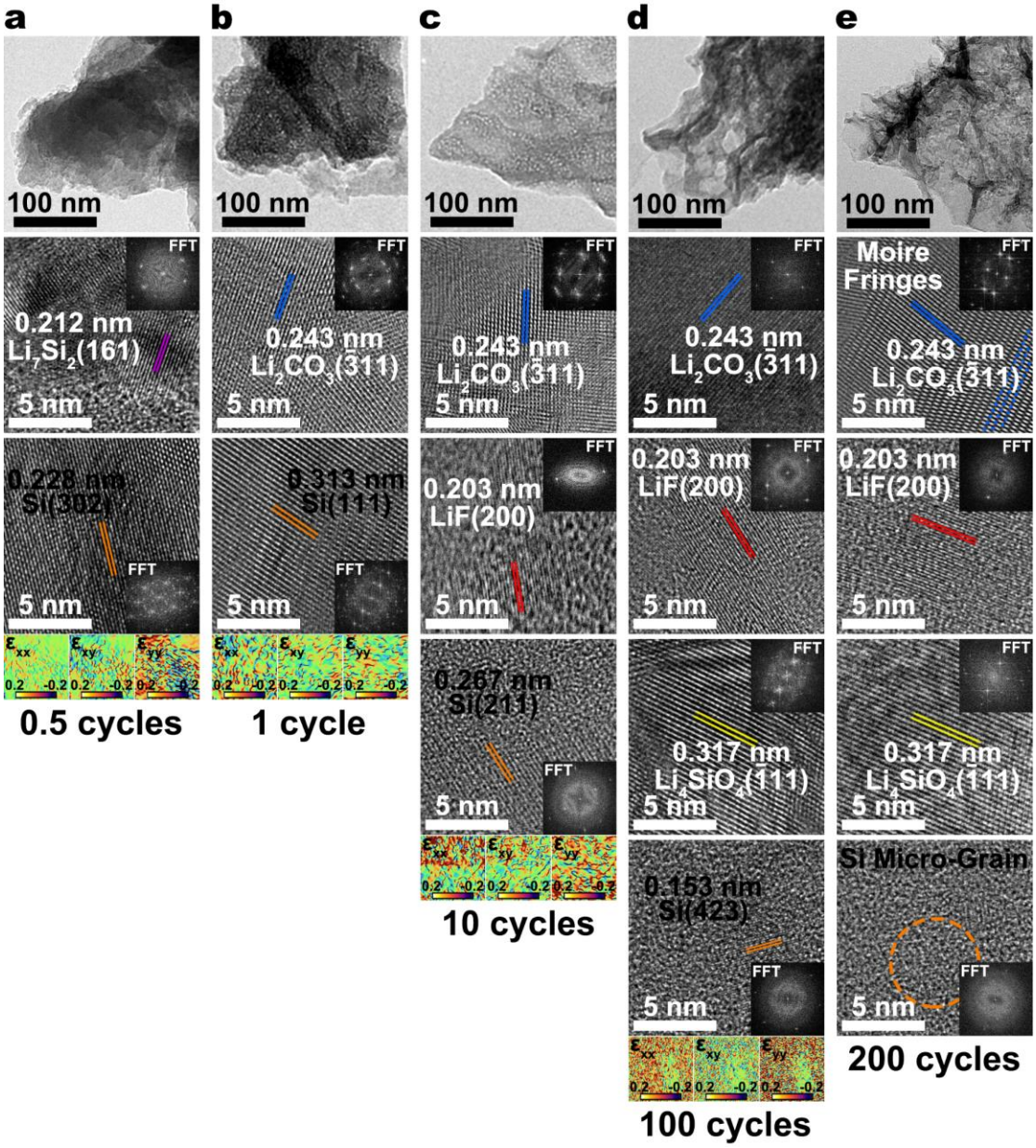

Fig. S45. AC-TEM characterization of SCNS-1100 after cycling. a-e, The morphology, composition and structure of SCNS-1100 were characterized at the ultramicro level by TEM and HRTEM (with FFT) after 0.5 (**a**), 1 (**b**), 10 (**c**), 100 (**d**) and 200 (**e**) cycles, respectively. In particular, the crystallographic composition and evolution of the SEI and Si phase were observed with emphasis to figure out the correlation between the two and the electrochemical performance of SCNS-1100. In addition, the ε_{xx}, ε_{xy} and ε_{yy} microstrain distributions of the HRTEM with crystalline Si were visualized by the GPA method to observe the pinning solidity of the crystalline phases in order to determine the cyclic mechanical properties of SCNS-1100.

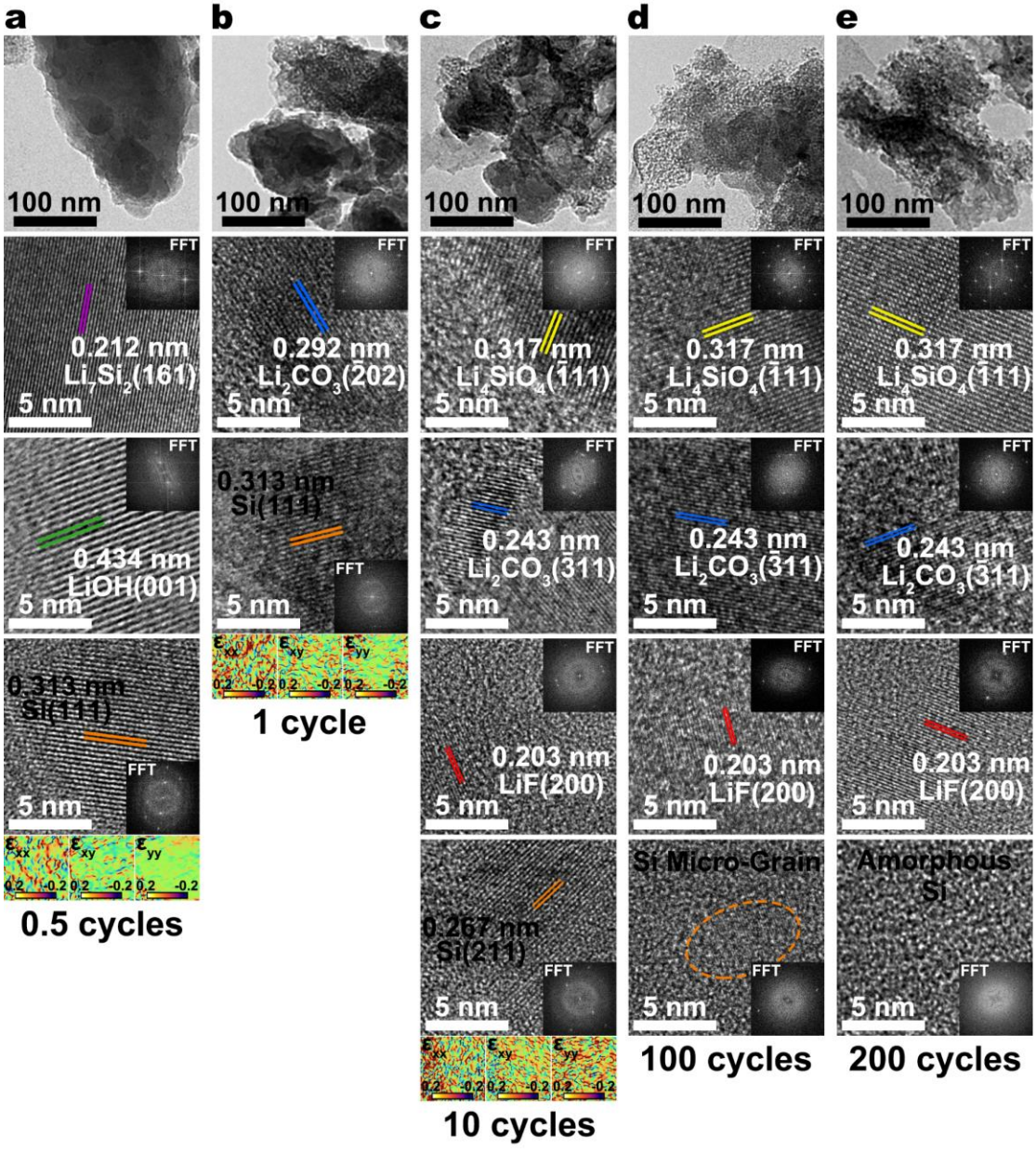

Fig. S46. AC-TEM characterization of SCNS-1200 after cycling. a-e, The morphology, composition and structure of SCNS-1200 were characterized at the ultramicro level by TEM and HRTEM (with FFT) after 0.5 (**a**), 1 (**b**), 10 (**c**), 100 (**d**) and 200 (**e**) cycles, respectively. In particular, the crystallographic composition and evolution of the SEI and Si phase were observed with emphasis to figure out the correlation between the two and the electrochemical performance of SCNS-1200. In addition, the ε_{xx}, ε_{xy} and ε_{yy} microstrain distributions of the HRTEM with crystalline Si were visualized by the GPA method to observe the pinning solidity of the crystalline phases in order to determine the cyclic mechanical properties of SCNS-1200.

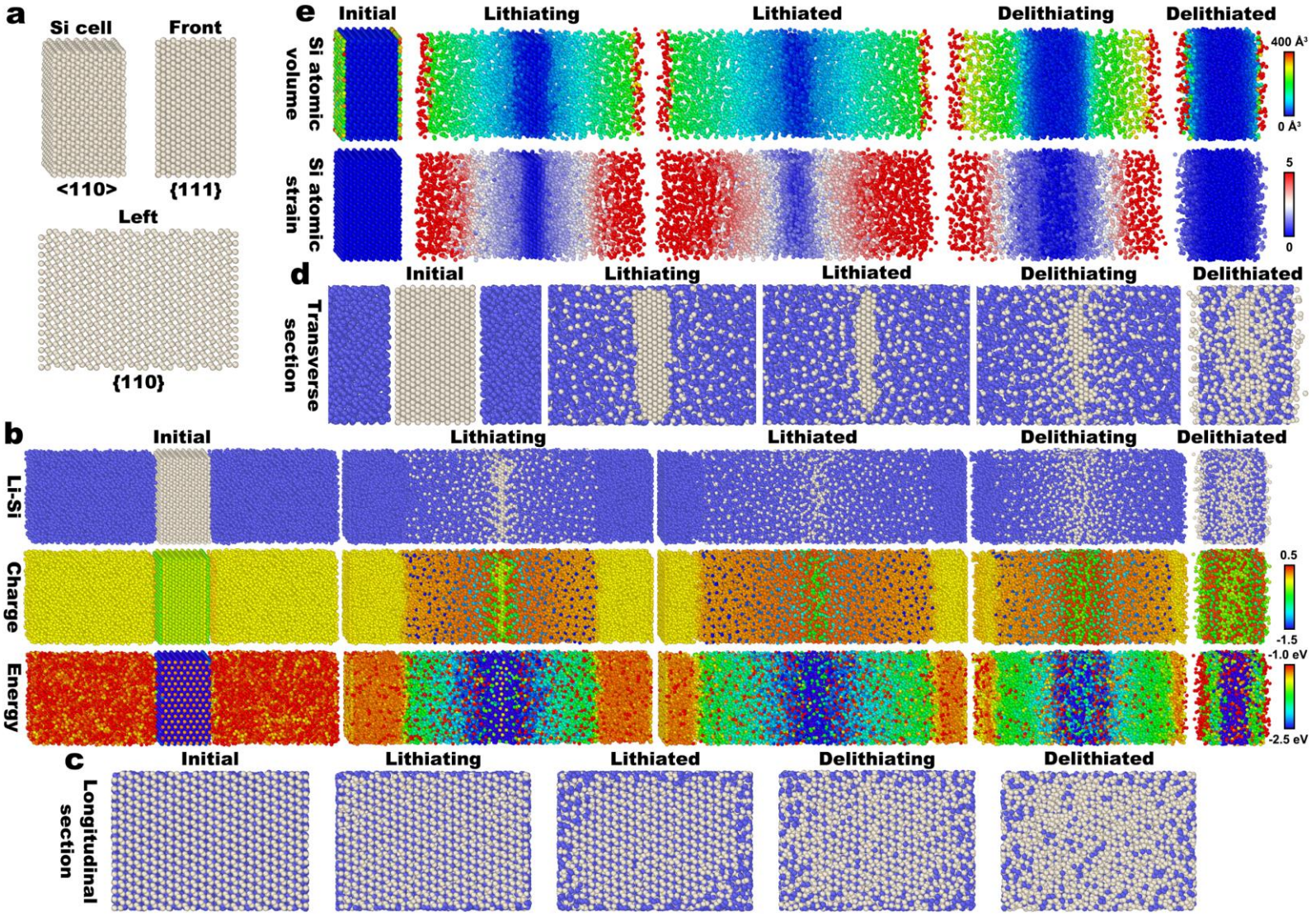
a
Si cell
Front
<110>
{111}
Left
{110}
e
Initial
Lithiating
Lithiated
Delithiating
Delithiated
Si atomic volume
400 Å³
0 Å³
Si atomic strain
5
0
d
Transverse section
b
Li-Si
Charge
0.5
-1.5
Energy
-1.0 eV
-2.5 eV
c
Longitudinal section

Fig. S47. Molecular dynamics simulation demonstration of the lithiation/delithiation for silicon single crystal. a, 3D model of the Si cell (Si <110> along the y-axis), and its front (Si {111}) and left views (Si {110}). **b,** Lithiation and delithiation of the Si cell encompasses changes in model (Li-Si), charge (in units of multiple of electron charge where 1.0 is a proton) and energy (kinetic + potential energy). **c-d,** Longitudinal (**c**) and transverse (**d**) sections for different states at the center of the Li-Si model. **e,** Si atomic volume and strain at different stages of the lithiation/delithiation.

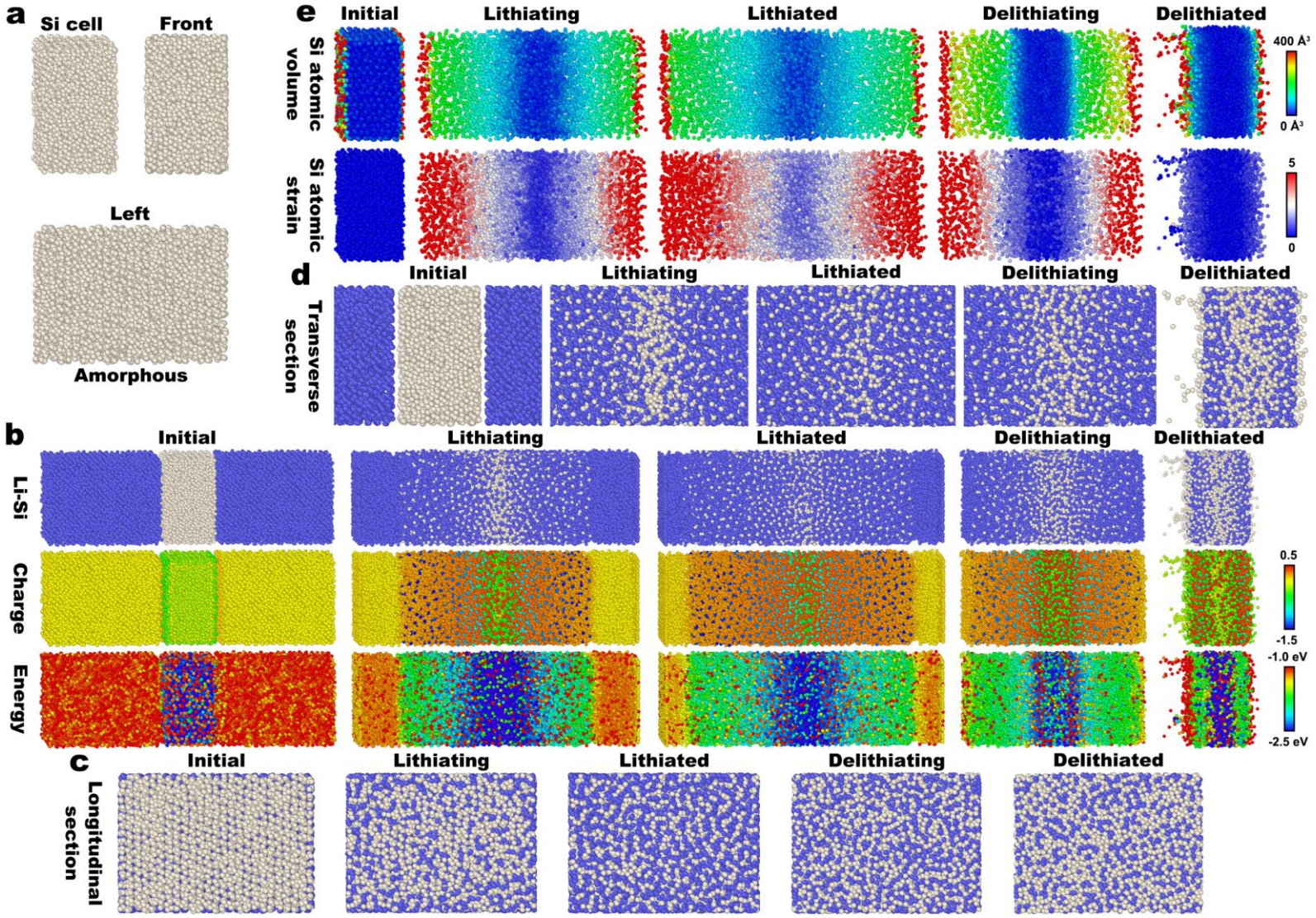
a
Si cell
Front
Left
Amorphous
e
Initial
Lithiating
Lithiated
Delithiating
Delithiated
Si atomic volume
400 Å³
0 Å³
Si atomic strain
5
0
d
Transverse section
b
Li-Si
Charge
Energy
0.5
-1.5
-1.0 eV
-2.5 eV
c
Longitudinal section

Fig. S48. Molecular dynamics simulation demonstration of the lithiation/delithiation for amorphous silicon. a, 3D model of the Si cell, and its front and left views. **b,** Lithiation and delithiation of the Si cell encompasses changes in model (Li-Si), charge (in units of multiple of electron charge where 1.0 is a proton) and energy (kinetic + potential energy). **c-d,** Longitudinal (**c**) and transverse (**d**) sections for different states at the center of the Li-Si model. **e,** Si atomic volume and strain at different stages of the lithiation/delithiation.

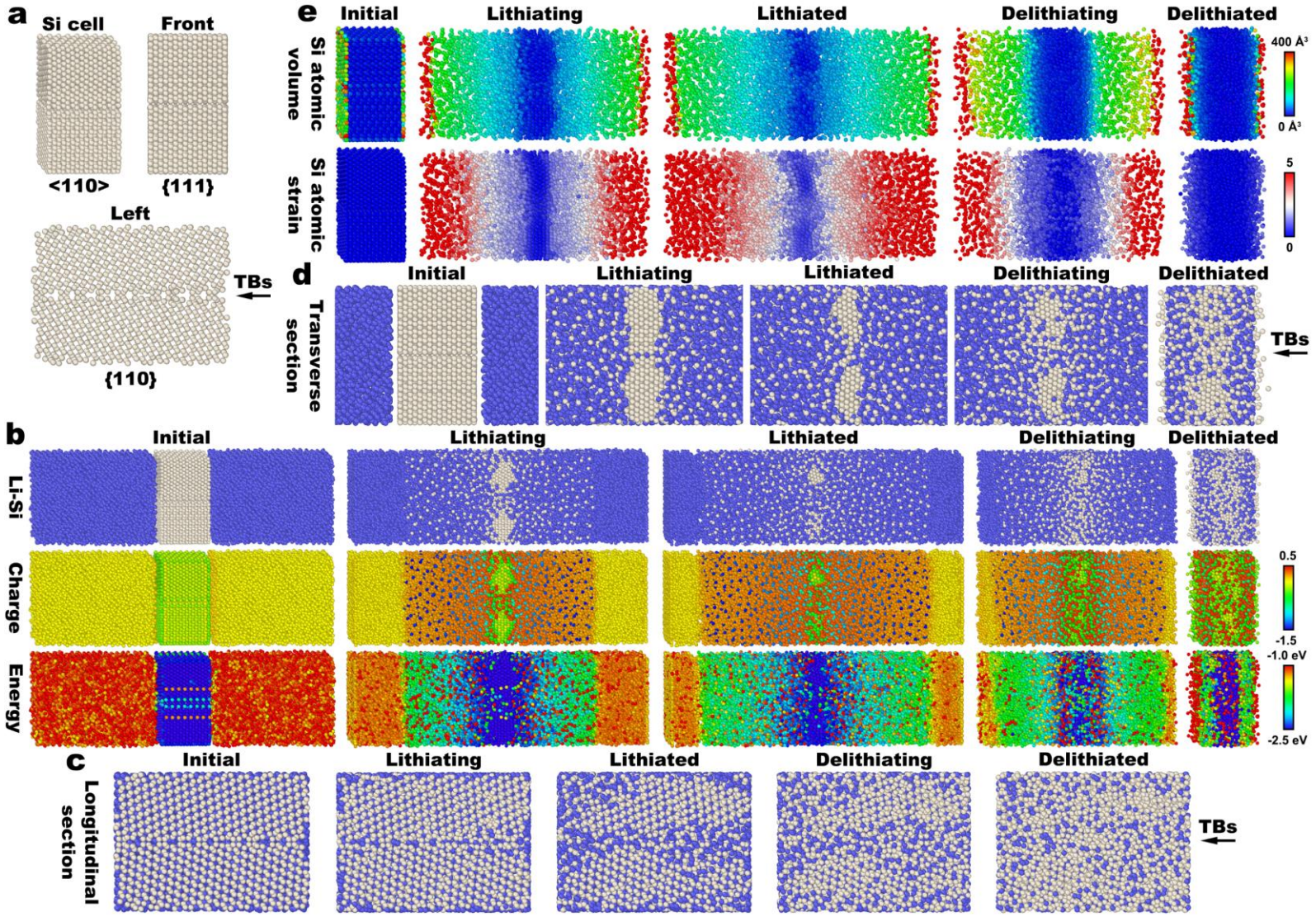
a
Si cell
Front
<110>
{111}
Left
TBs
{110}
e
Initial
Lithiating
Lithiated
Delithiating
Delithiated
Si atomic volume
400 Å³
0 Å³
Si atomic strain
5
0
d
Transverse section
TBs
b
Li-Si
Charge
Energy
0.5
-1.5
-1.0 eV
-2.5 eV
c
Longitudinal section
TBs

Fig. S49. Molecular dynamics simulation demonstration of the lithiation/delithiation for the TBs-containing silicon crystal. a, 3D model of the Si cell (Si <110> along the y-axis), and its front (Si {111}) and left views (Si {110}). **b,** Lithiation and delithiation of the Si cell encompasses changes in model (Li-Si), charge (in units of multiple of electron charge where 1.0 is a proton) and energy (kinetic + potential energy). **c-d,** Longitudinal (**c**) and transverse (**d**) sections for different states at the center of the Li-Si model. **e,** Si atomic volume and strain at different stages of the lithiation/delithiation.

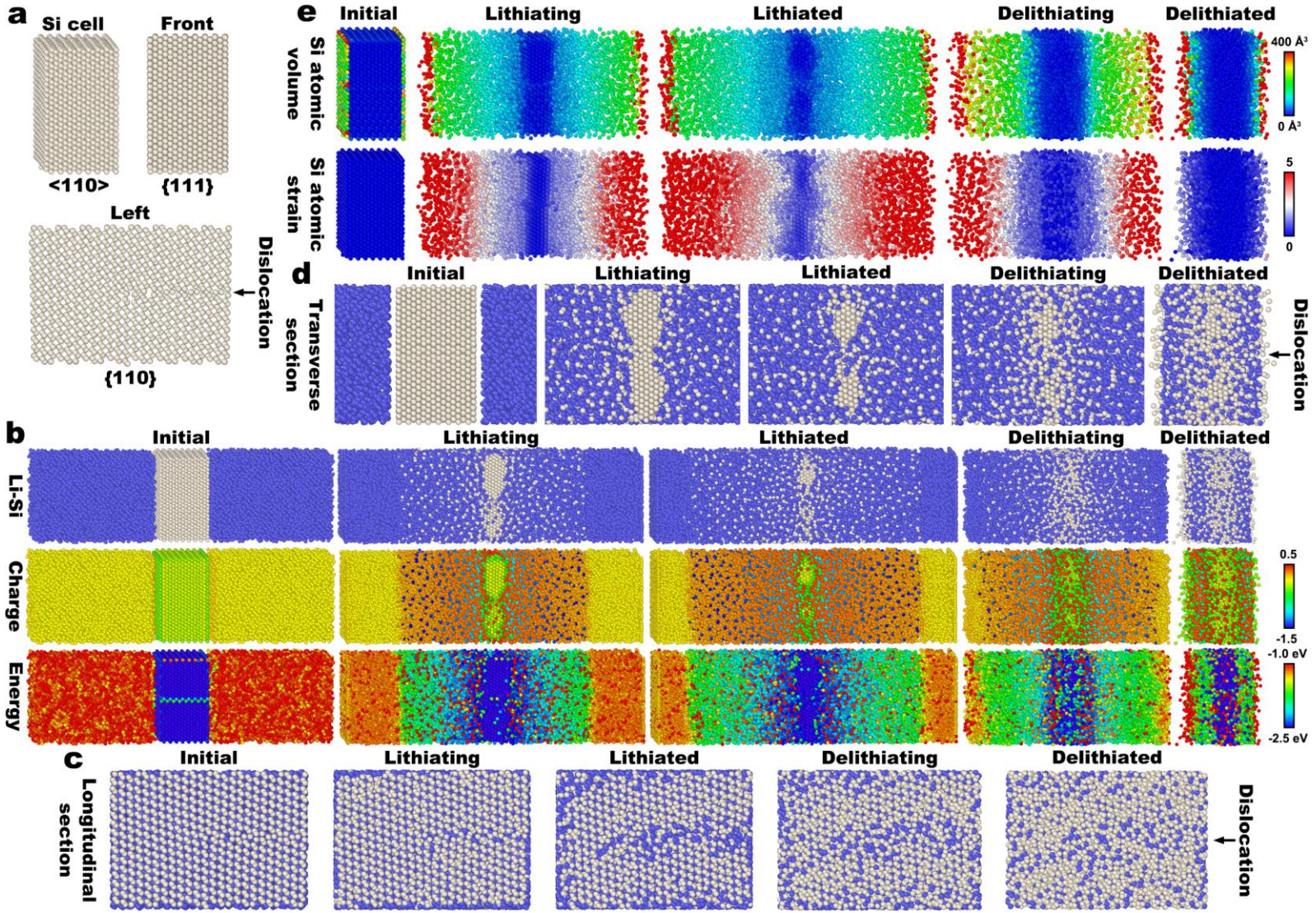
a
Si cell
Front
<110>
{111}
Left
{110}
Dislocation
e
Initial
Lithiating
Lithiated
Delithiating
Delithiated
Si atomic volume
400 Å³
0 Å³
Si atomic strain
5
0
d
Transverse section
Dislocation
b
Li-Si
Charge
Energy
0.5
-1.5
-1.0 eV
-2.5 eV
c
Longitudinal section
Dislocation

Fig. S50. Molecular dynamics simulation demonstration of the lithiation/delithiation for the dislocation-containing silicon crystal. a, 3D model of the Si cell (Si <110> along the y-axis), and its front (Si {111}) and left views (Si {110}). **b,** Lithiation and delithiation of the Si cell encompasses changes in model (Li-Si), charge (in units of multiple of electron charge where 1.0 is a proton) and energy (kinetic + potential energy). **c-d,** Longitudinal (**c**) and transverse (**d**) sections for different states at the center of the Li-Si model. **e,** Si atomic volume and strain at different stages of the lithiation/delithiation.

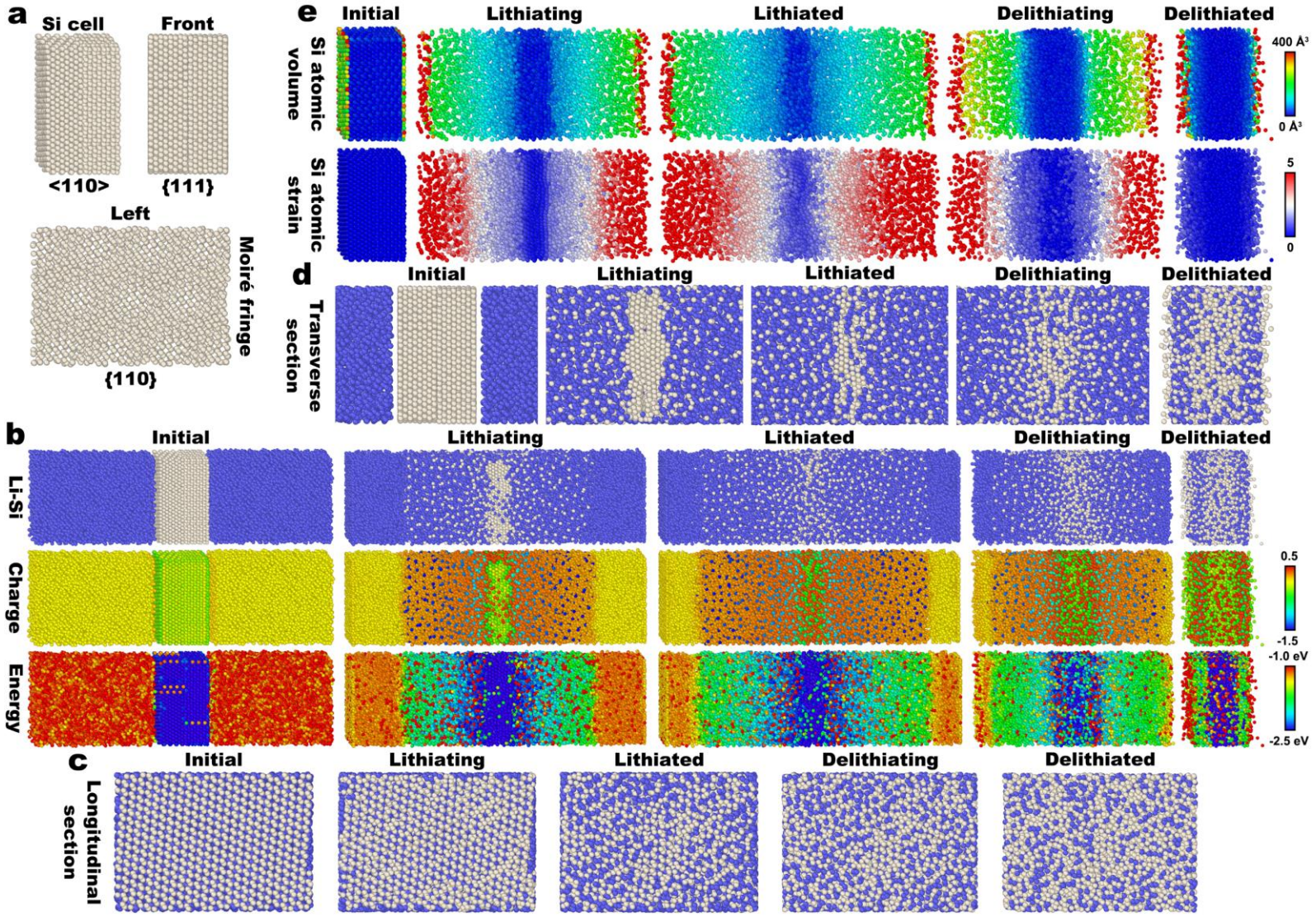
a
Si cell
Front
<110>
{111}
Left
Moiré fringe
{110}
e
Initial
Lithiating
Lithiated
Delithiating
Delithiated
Si atomic volume
400 Å³
0 Å³
Si atomic strain
5
0
d
Transverse section
b
Li-Si
Charge
Energy
0.5
-1.5
-1.0 eV
-2.5 eV
c
Longitudinal section

Fig. S51. Molecular dynamics simulation demonstration of the lithiation/delithiation for the silicon Moiré-crystal. a, 3D model of the Si cell (Si <110> along the y-axis), and its front (Si {111}) and left views (Si {110}). **b,** Lithiation and delithiation of the Si cell encompasses changes in model (Li-Si), charge (in units of multiple of electron charge where 1.0 is a proton) and energy (kinetic + potential energy). **c-d,** Longitudinal (**c**) and transverse (**d**) sections for different states at the center of the Li-Si model. **e,** Si atomic volume and strain at different stages of the lithiation/delithiation.

Supplementary Tables

Table S1. Elemental test results of SCNS by ICP-OES and high frequency infrared C-S analyzer.

Element	Content (wt%)	Element	Content (wt%)
Ag	null	Mo	null
Al	0.17	Na	0.034
As	<0.0001	Ni	0.0045
Ba	0.0001	P	0.0039
Be	null	Pb	0.0005
Ca	0.012	S	0.0026
Cd	<0.0001	Sb	0.0003
Ce	<0.0001	Sc	<0.0001
Co	<0.0001	Se	null
Cr	0.0002	Sn	0.0001
Cu	0.0017	Sr	<0.0001
Fe	0.0093	Ti	0.0052
Hg	null	V	0.0002
K	0.0016	W	<0.0001
La	<0.0001	Y	<0.0001
Li	0.0001	Zn	0.0008
Mg	0.0022	Zr	0.0002
Mn	0.0011	C	1.07

Table S2. Oxygen content of Si-raw and SCNS measured by ONH836 Analyzer and EDS, respectively.

Material	ONH836 Analyzer (wt%)	EDS (wt%)
Si-raw	28.30[1]	29.92[1]

SCNS	3.26	3.83

Table S3. The crystallinity of SCNS, SCNS-800, SCNS-900, SCNS-1000, SCNS-1100 and SCNS-1200 obtained by fitting XRD data.

Sample	Crystallinity (%)	R (%)
SCNS	46.11	6.98
SCNS-800	72.27	9.88
SCNS-900	75.94	9.66
SCNS-1000	78.75	10.12
SCNS-1100	81.19	9.44
SCNS-1200	82.92	9.06

Table S4. The grain size and microstrain of SCNS, SCNS-800, SCNS-900, SCNS-1000, SCNS-1100 and SCNS-1200 obtained by fitting XRD data.

Sample	Grain size (nm)	Strain (%)
SCNS	17.2	0.142
SCNS-800	51	0.212
SCNS-900	48.6	0.141
SCNS-1000	70	0.129
SCNS-1100	83.2	0.106
SCNS-1200	104	0.072

Table S5. The crystallinity of SCNS, SCNS-800, SCNS-900, SCNS-1000, SCNS-1100 and SCNS-1200 obtained by fitting Raman data.

Sample	Crystallinity (%)	COD (R^2)

SCNS	52.59	97.86%
SCNS-800	69.36	98.35%
SCNS-900	72.55	99.67%
SCNS-1000	76.16	99.85%
SCNS-1100	80.35	98.30%
SCNS-1200	85.08	98.84%

Table S6. Half-cell discharge/charge data of Si-raw, SCNS, SCNS-800, SCNS-900, SCNS-1000, SCNS-1100 and SCNS-1200 after different cycles respectively.

Sample	Initial Discharge Capacity (mAh g^{-1})	Initial Charge Capacity (mAh g^{-1})	Initial Coulombic Efficiency (%)	9th Reversible Capacity (mAh g^{-1})	200th Reversible Capacity (mAh g^{-1})
Si-raw	1926.8	1008.0	52.31	208.3	6.8
SCNS	3347.2	2593.4	77.50	2286.1	201.1
SCNS-800	3287.5	2565.4	78.04	1987.4	1101.3
SCNS-900	3752.8	3112.2	82.93	2764.3	2180.9
SCNS-1000	3351.7	2651.8	79.12	2249.8	1002.2
SCNS-1100	3209.3	2481.4	77.32	2272.2	1734.2
SCNS-1200	2987.8	2269.2	75.95	1776.5	1245.2

Table S7. The impedance and D_{Li}^{+} of SCNS, SCNS-800, SCNS-900, SCNS-1000, SCNS-1100 and SCNS-1200 electrodes were obtained by fitting EIS data. σ is the slope of the Zre-$\omega^{-1/2}$ curve used for the calculation of D_{Li}^{+}.

Sample	R_s (Ω)	R_{ct} (Ω)	σ	D_{Li}^{+} (m^2 s^{-1})
SCNS	1.90	49.11	4798.50	$3.6*10^{-23}$

SCNS-800	2.80	137.70	300.63	$9.2*10^{-21}$
SCNS-900	1.71	60.21	2225.61	$1.7*10^{-22}$
SCNS-1000	1.17	75.33	2417.00	$1.4*10^{-22}$
SCNS-1100	1.37	89.72	2037.87	$2.0*10^{-22}$
SCNS-1200	1.23	80.19	2647.22	$1.2*10^{-22}$

Table S8. Half-cell discharge/charge data of SCNS-900 at various current densities.

Cycle	Current Density ($A\ g^{-1}$)	Discharge Capacity ($mAh\ g^{-1}$)	Charge Capacity ($mAh\ g^{-1}$)	Coulombic Efficiency (%)
1st	0.2	3835.5	3164.4	82.50
5th	0.2	3364.0	3305.7	98.27
15th	0.4	3230.7	3183.0	98.52
25th	0.8	2986.4	2950.4	98.79
35th	2.0	2577.0	2551.9	99.03
45th	4.0	1898.0	1881.6	99.14
55th	8.0	1144.0	1136.9	99.38
65th	0.2	2928.0	2870.6	98.04

Table S9. Half-cell discharge/charge data for SCNS-900 at 2.0 and 4.0 $A\ g^{-1}$, respectively.

Current Density ($A\ g^{-1}$)	Initial Discharge Capacity ($mAh\ g^{-1}$)	Initial Charge Capacity ($mAh\ g^{-1}$)	Initial Coulombic Efficiency (%)	9th Reversible Capacity ($mAh\ g^{-1}$)	300th Reversible Capacity ($mAh\ g^{-1}$)
2.0	3670.1	3041.1	82.86	2462.6	1648.9
4.0	3653.8	2990.0	81.83	2163.6	1159.4

Table S10. Electrochemical performance of SCNS-900 in this manuscript versus other Si-based anodes in the literature.

Specific capacity (mAh g^{-1})	Cycle numbers	Slurrying ratio (Active substance: Binder: Conductive agent)	Current density (A g^{-1})	Component	Ref.
~1000	200	7:1:2	0.5	MXene/Si/CNT	[2]
~1300	300	6:2:2	0.04	Si/C	[3]
2056	300	5:2:3	0.2	Si@CNT/C	[4]
1473.3	400	8:1:1	0.2	Si/C	[5]
925.4	100	7:2:1	1.0	C-SiO_x@Si/rGO	[6]
1154	150	7:1:2	0.2	Si/$Ti_3C_2T_x$	[7]
2041.9	200	7:2:1	0.84	Nano Si with N-DHF	[8]
~1500	200	7:1:2	0.5	Si/C	[9]
1600	200	7:2:1	1.0	Si/MgF_2	[10]
1983.9	300	8:1:1	0.8	Pure Si	This work

Table S11. Full-cell charge/discharge data for SCNS-900 at 0.1 and 0.5 C, respectively.

Charge/ Discharge Rate (C)	Initial Discharge Capacity (mAh g^{-1})	Initial Charge Capacity (mAh g^{-1})	Initial Coulombic Efficiency (%)	20th Reversible Capacity (mAh g^{-1})
0.1	135.0	173.0	78.03	104.1
0.5	129.9	169.6	76.61	100.8

Table S12. Si, C, O, F and P contents of the SCNS-900 electrodes measured by EDS after 0, 10, 100 and 200 cycles, respectively.

Cycles	Si Content (At%)	C Content (At%)	O Content (At%)	F Content (At%)	P Content (At%)
0	47.2	37.5	15.1	Null	Null
10	9.5	45.3	25.7	17.5	1.9
100	5.3	35.8	39.1	18.5	1.2
200	14.3	0.2	42.6	37.8	5.0

Table S13. Si, C, O, F and P contents of the SCNS electrodes measured by EDS after 0, 10, 100 and 200 cycles, respectively.

Cycles	Si Content (At%)	C Content (At%)	O Content (At%)	F Content (At%)	P Content (At%)
0	40.7	47.5	11.9	Null	Null
10	14.6	0.3	49.4	30.8	4.8
100	7.1	34.5	42.1	14.9	1.3
200	5.6	35.7	39.8	17.5	1.4

Table S14. Si, C, O, F and P contents of the SCNS-800 electrodes measured by EDS after 0, 10, 100 and 200 cycles, respectively.

Cycles	Si Content (At%)	C Content (At%)	O Content (At%)	F Content (At%)	P Content (At%)
0	37.3	50.0	12.7	Null	Null
10	21.6	0.2	54.2	21.3	2.6
100	10.3	39.7	31.6	16.4	1.9
200	5.4	31.7	38.8	22.6	1.4

Table S15. Si, C, O, F and P contents of the SCNS-1000 electrodes measured by EDS after 0, 10, 100 and 200 cycles, respectively.

Cycles	Si Content	C Content	O Content	F Content	P Content

	(At%)	(At%)	(At%)	(At%)	(At%)
0	40.7	44.8	14.5	Null	Null
10	12.5	33.7	35.5	17.0	1.3
100	6.6	33.4	40.5	17.8	1.6
200	4.8	33.8	36.3	23.8	1.3

Table S16. Si, C, O, F and P contents of the SCNS-1100 electrodes measured by EDS after 0, 10, 100 and 200 cycles, respectively.

Cycles	Si Content (At%)	C Content (At%)	O Content (At%)	F Content (At%)	P Content (At%)
0	35.2	50.8	14.0	Null	Null
10	15.3	36.8	31.1	14.9	1.9
100	11.0	36.0	30.3	21.0	1.6
200	6.8	34.2	39.5	18.0	1.4

Table S17. Si, C, O, F and P contents of the SCNS-1200 electrodes measured by EDS after 0, 10, 100 and 200 cycles, respectively.

Cycles	Si Content (At%)	C Content (At%)	O Content (At%)	F Content (At%)	P Content (At%)
0	43.9	42.8	13.3	Null	Null
10	13.5	35.5	31.4	18.2	1.4
100	8.5	34.3	31.4	23.9	1.8
200	6.1	35.9	39.5	17.3	1.2

Table S18. The active substance loading in the electrodes of the samples.

Sample	Active substance loading (mg cm^{-2})
Si-raw	0.41-0.82
SCNS	0.40-0.86

SCNS-800	0.40-0.80
SCNS-900	0.45-0.76
SCNS-1000	0.44-0.70
SCNS-1100	0.40-0.78
SCNS-1200	0.41-0.74

Supplementary References

[1] T. Hu, H. Zhou, X. Zhou, J. Tang, S. Chen, S. Fan, C. Luo, Y. Ma, J. Yang, *Small.* **2023,** *19* (7), e2204690.
[2] S. Liu, X. Zhang, P. Yan, R. Cheng, Y. Tang, M. Cui, B. Wang, L. Zhang, X. Wang, Y. Jiang, L. Wang, H. Yu, *ACS Nano.* **2019,** *13* (8), 8854-8864.
[3] H. J. Kwon, J. Y. Hwang, H. J. Shin, M. G. Jeong, K. Y. Chung, Y. K. Sun, H. G. Jung, *Nano Lett.* **2020,** *20* (1), 625-635.
[4] H. Wang, J. Fu, C. Wang, J. Wang, A. Yang, C. Li, Q. Sun, Y. Cui, H. Li, *Energy & Environmental Science.* **2020,** *13* (3), 848-858.
[5] Y. An, Y. Tian, Y. Zhang, C. Wei, L. Tan, C. Zhang, N. Cui, S. Xiong, J. Feng, Y. Qian, *ACS Nano.* **2020,** *14* (12), 17574-17588.
[6] T. Meng, B. Li, Q. Wang, J. Hao, B. Huang, F. L. Gu, H. Xu, P. Liu, Y. Tong, *ACS Nano.* **2020,** *14* (6), 7066-7076.
[7] M. Xia, B. Chen, F. Gu, L. Zu, M. Xu, Y. Feng, Z. Wang, H. Zhang, C. Zhang, J. Yang, *ACS Nano.* **2020,** *14* (4), 5111-5120.
[8] Z. Cao, X. Zheng, Q. Qu, Y. Huang, H. Zheng, *Adv Mater.* **2021,** *33* (38), e2103178.
[9] R. Zhu, Z. Wang, X. Hu, X. Liu, H. Wang, *Advanced Functional Materials.* **2021,** *31* (33), 2101487.
[10] S. Mei, B. Xiang, S. Guo, J. Deng, J. Fu, X. Zhang, Y. Zheng, B. Gao, K. Huo, P. K. Chu, *Advanced Functional Materials.* **2023,** *34* (5), 2301217.